# Computer modelling of Pure and Doped Titanium Dioxide in Anatase Structure

A thesis presented
By

*Malili Gideon Matshaba*

to

**The Department of Physics**

in fulfilment of the requirements

for the degree of

**Master of Science**

in the subject of

**Physics**

**University of Limpopo**

**Supervisor: Prof. P.E. Ngoepe**
RSA, Sovenga

[2006]

# Declaration

I declare that the dissertation hereby submitted to the University of Limpopo for the degree of Master of Science has not been previously submitted by me for a degree at this or any University, that it is my own work in design and in execution, and that all materials contained therein has been duly acknowledged.

Signature of the Author……

Malili Gideon Matshaba

# Dedication

To my mother

Ramokone, my

two brothers (Nkgaru and Lesiba) and three sisters (Matome,

Mokgadi and Khomotšo)

Kea leboga ditau.

# Acknowledgements

I would like to express my gratitude to my supervisor Professor P.E. Ngoepe whose help, stimulating suggestions and encouragement helped me in all the time of the research for and writing of this thesis.

I am deeply indebted to my colleagues of the Material Modelling Centre (MMC), where all my calculations in this thesis were done. Thanks to the University of Limpopo community for giving me a wonderful environment through out my research study.

I want to thank National Research Foundation (NRF) and Eskom for financial assistance since the beginning of my research. Without them I don't think I could have done my research.

Lastly, I would like to give my special thanks to my dear mother Ramokone Ileen Matshaba, and all members of the family for their support throughout my study. I also give thanks to my sister Matome and my brother in law Kgokoloa for their encouragement of studying in the University of Limpopo.

Most of all, I thank the Mighty Creator for giving me good life throughout my study.

# Abstract

The structural, electronic and optical properties of titanium dioxide ($TiO_2$) in anatase phase have been studied by first-principle self-consistent local density approximation. Norm-conserving pseudopotentials were utilized and wavefunctions were represented by using plane wave basis set. Calculated structural parameters of anatase within LDA agree well with the experimental parameters. Optimized atomic positions of $TiO_2$ are the same as the original positions. Densities of states were calculated and they are instructive to the understanding of the system. Pressure dependence structure shows high compressibility along the c parameter. The bulk modulus of $TiO_2$ was calculated and was found to be 178.9 GPa which agrees well with the experimental value which is 179.0 GPa.

We have doped anatase with transition metals (Pt, Au, Ag and Pd) to study their effect on structural and optical properties of $TiO_2$. Doping decreases the band gap of the structure and increases the optical properties (absorption and reflectivity) of pure anatase in the visible region.

# Contents

# List of figures

# List of Tables

# Chapter 1
# INTRODUCTION

## 1.1 General introduction

Titanium dioxide is an oxide, which forms three distinct polymorphs: rutile, anatase and brookite. Its chemical formula is $TiO_2$ and its composition is 59.94% of titanium and 40.06% oxygen which makes 100.00% $TiO_2$. Anatase, a titanium oxide mineral, was first found in the Buckwheat Dolomite by W.B. Thomas and was later reported by Frondel (1972) and Peters et al. (1983). It is reported to be deep blue, with the morphological characteristics of common anatase, but its identification to date is only visual (http://simplethinking.com/dunn/ch22/anatase.stm). Figure1.1 shows the rock of anatase. Titanium dioxide is chemically stable, non-hazardous and resistant to extreme temperature and weather. It is inexpensive and widely available commercially (Barbe et al 1997). Anatase and rutile crystal structures consist of chains of $TiO_2$ octahedra. These octahedra are more distorted in anatase-$TiO_2$ than in rutile-$TiO_2$, resulting in different structures and distinct physical and chemical properties (Fahmi et al 1993). Anatase has attracted a great deal of interest in connection with technological applications (Berger et al 1993, Gratzel 1991). Anatase is intensively studied for photocatalysis and photo electrochemical applications and is more actively investigated. It has been pointed out that the fermi level in anatase is higher than that of rutile by about 0.1eV (Maruska et al 1978). It is also known that anatase plays a key role in the injection process of photochemical solar cells with high conversion efficiency (Gratzel 1991).

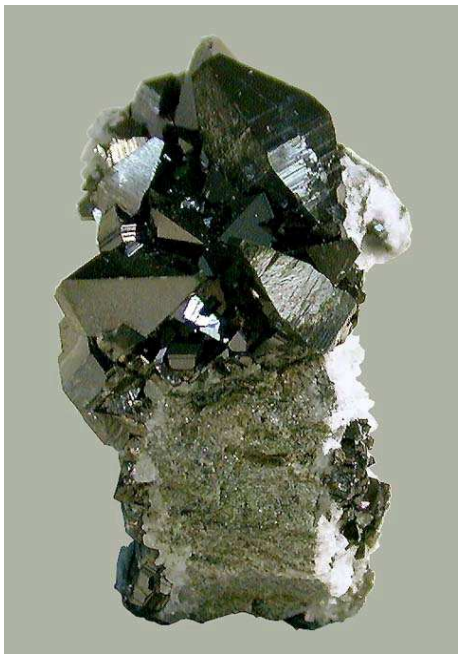

**Figure 1.1: Titanium dioxide ($TiO_2$) anatase rock.**

There are two routes for the production of $TiO_2$ pigments namely, sulphate and chloride route. Sulphate process: In the sulphite process, ilmenite is directly reacted with sulphuric acid to produce titanium sulphate and iron sulphate. The Titanium sulphate is subjected to selective thermal hydrolysis to produce hydrated titanium dioxide. This is further washed and calcined to produce titanium dioxide pigment. Sulphite process produce anatase and rutile grade.

## 1.2 Structural properties

Formally, the titanium dioxide ($TiO_2$) oxides are made of $d^o$ titanium ions (+IV) at the centre of octahedra of six $O^{2-}$ ions. Each oxygen atom has three titanium neighbours and therefore belongs to three different octahedra. Three parameters of anatase structure: the two Ti-O bond lengths and the angle 2θ (the largest Ti-O-Ti angle, the smallest O-Ti-O angle which concerns one apical and one equatorial Ti-O bond is α=θ) are defined in figure1.2.

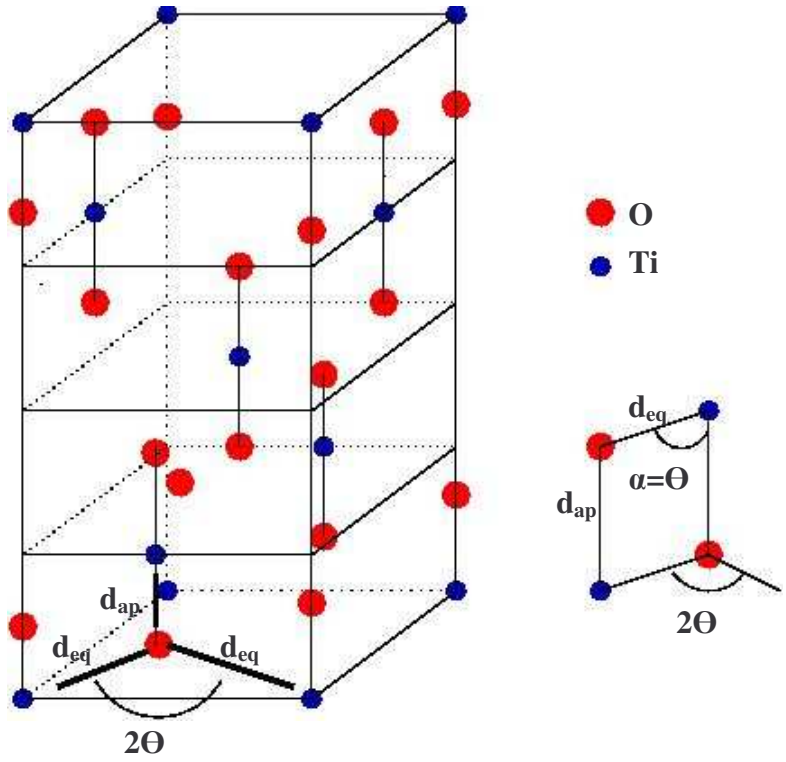


**Figure 1.2: Definition of parameters in anatase structure (After Fahmi et al 1993).**

Conversion from our parameters to the crystallographic ones is the following:

$a = 2d_{eq}\sin\theta = 3.784$ Å,

$c = 4(d_{ap} + d_{eq}\cos\theta) = 9.515$ Å,

$$u = \frac{d_{ap}}{4(d_{ap} + d_{eq}\cos\theta} = 0.208 \text{ Å}.$$

The cell unit volume (which contains two $TiO_2$ units; half of the quadratic cell) is

$$V = \frac{a^2 c}{2} = 8\left(d_{ap} + d_{eq}\cos\theta\right)d^2{}_{eq}\sin^2\theta.$$

The cell volume may be simplified as $V = 4d^3\left(1+\cos\theta\right)\sin^2\theta$, which has a maximum value for $2\theta = 140.2^0$, a value which is close to the experimental value $156^0$.

The basic unit-cell structure of anatase is shown in figure 1.3 and figure1.4 shows the structure in the form of polyhedron (shows how atoms are bonded to each other).

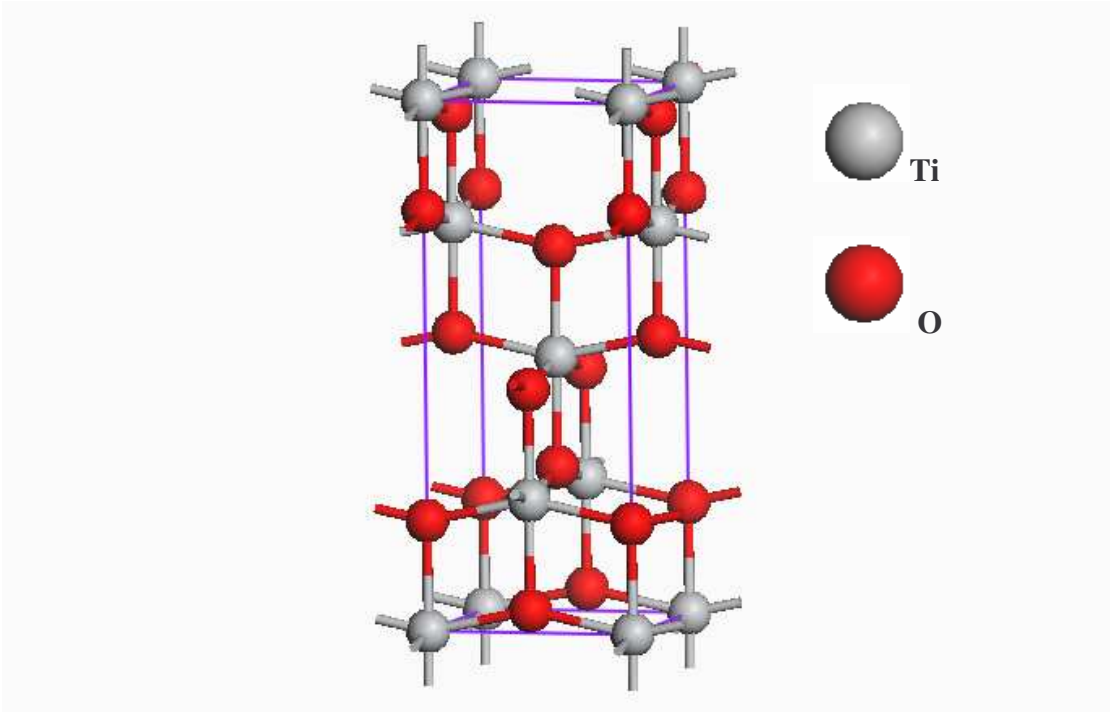


**Figure 1.3: Conventional unit-cell for $TiO_2$ in anatase phase.**

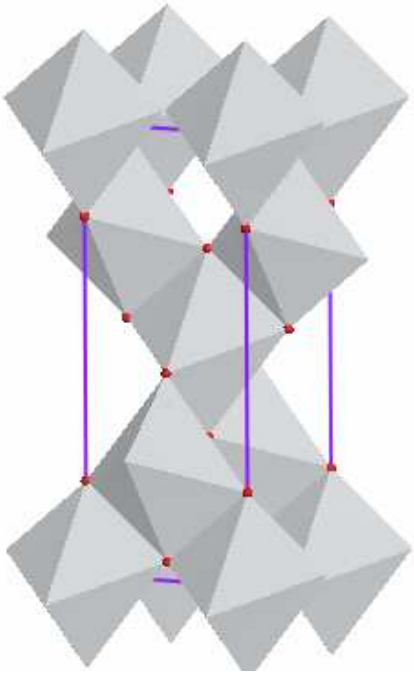

**Figure 1.4: Polyhedron structure of $TiO_2$ anatase structure.**

The crystal parameters, the Ti-O interatomic distances, and the O-Ti-O bond angles for the anatase are summarized in table1.1.

**Table1.1Physical properties of $TiO_2$ anatase phase**

| | |
|---|---|
| Crystal structure | Tetragonal |
| Lattice constants a = b (Å) | 3.784 |
| Lattice constant c (Å) | 9.515 |
| Colour | Brown to black (also yellow to blue) |
| Point group | 4/mmm |
| Space group | I41/amd |
| Volume ($Å^3$) | 136.25 |
| Density ($g/cm^3$) | 3.895 |
| Molar volume | 20.156 |
| Hardness | 5.5-6 |
| Specific gravity | 3.8-3.9 |
| Streak | white |
| Ti-O bond length | 1.937 (4) & 1.965 (2) |
| O-Ti-O bond angle | $77.7^0$ & $92.6^0$ |

## 1.3 Literature review

### 1.3.1 Titanium dioxide- Photoactive semiconductor

White pigment of titanium dioxide is used mostly as the best efficient in the market. About four million tons are produced annually for the use in long lasting coatings, plastics, ceramics adhesives or paper. The same material has been produced in photo-active grades as well. $TiO_2$ shows no absorption of any fraction of the visible light, thus it is not coloured. In the region of shorter wavelength a strong absorption of UV-radiation is observed. This is due to the promotion of an electron out of the valence band into the conductive band; titanium dioxide is a photo semi conductor. The band gap is 3.05eV (anatase modification). The electronic structure of a titanium dioxide crystal and possible points of modification /influence are shown in figure 1.5. Possible

points of influence /modification are marked with an arrow.

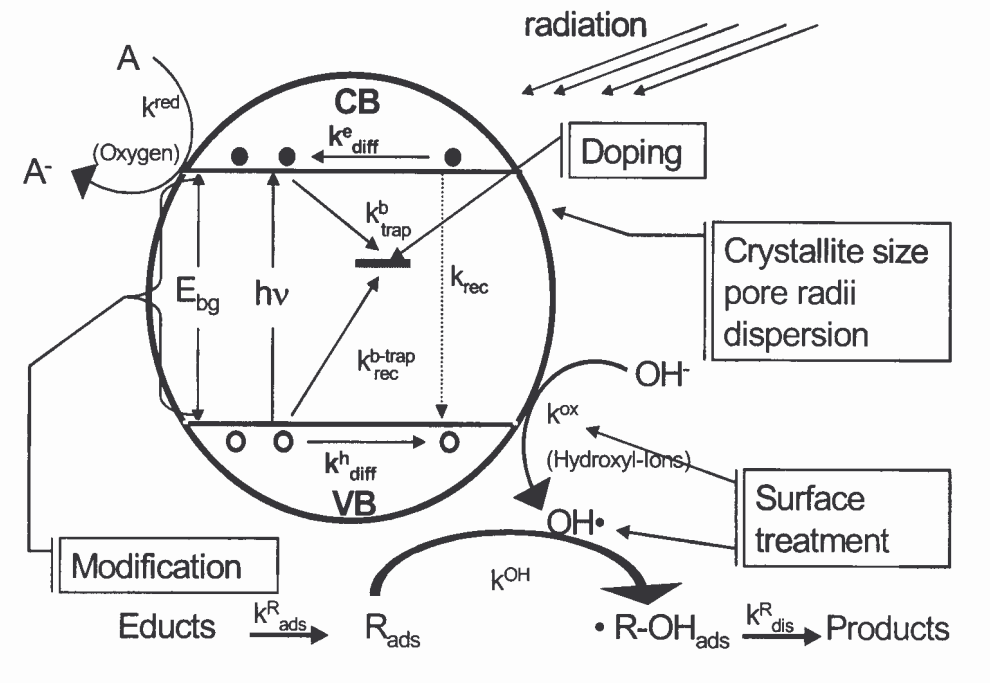


**Figure 1.5: Electronic structure of titanium dioxide (Ollis et al).**

Some uses of titanium dioxide are for solar cell. A solar cell is a device for converting energy from the sun into electricity. Atomic force Microscopy (AFM) has been used to view titanium dioxide solar cell topography and its nanocrystalline particles vary in sizes from 170 -470 nm. More details on AFM are found in the website below. (http://groups.msn.com/100Mexican/chm494specialprojecttitaniumdioxidesolarcells.msnw).

## 1.3.2 Doped $TiO_2$ anatase structure

Most work has been done on doping $TiO_2$ anatase with different kinds of elements. Niobium (Nb) doped anatase have been studied using combined transmission electron microscopy, Raman spectroscopy, X-ray diffraction and selected area electron diffraction analysis (Arbiol et al 2002). Their aim was to study the influence of Nb doping on $TiO_2$ anatase to rutile phase transition. They have found that niobium is segregated from the anatase structure before and during the phase transformation,

leading to the formation of NbO nanoclusters on the surface of the $TiO_2$ rutile nanoparticles.

Electronic structures of a room-temperature-diluted magnetic semiconductor: Co doped anatase $TiO_2$ have been investigated (Park et al 2002). They have obtained the half-metallic ground state for Co-doped $TiO_2$ with the carrier type of mainly Co 3d states. They have also found that Mn- and Fe- doped $TiO_2$ have the magnetic ground states, while Ni-doped $TiO_2$ has the paramagnetic ground states.

The effect of n-type carrier doping by Li intercalation on magnetism in undoped and Co-doped anatase $TiO_2$ was investigated (Park et al 2003). They have found that, by intercalation Li in $TiO_2$, Ti atoms have localized magnetic moments, 0.029 and 0.027μB for Li/Ti =0.125 and 0.25, respectively. For Co-doped $TiO_2$, nonmagnetic ground states are obtained for Li/Ti =0.067 and 0.133.

The ab initio calculations of Ge doped anatase $TiO_2$ were performed (Chen et al 2005) by using the full potential- linearized plane wave method (FP-LAPW). They have obtained the fully optimized structure. Density of states and band structures were calculated for the understanding of the system. Their DOS shows that their system is a half metallic.

Extended X-ray absorption fine structure (EXAFS) spectroscopy was used for the study of dopant segregation (Zn, Nb) in nanocrystalline anatase ($TiO_2$) (Bouchet et al 2003). They were investigating the different concentrations between 0.1 and 1 at. % Nanocrystalline powders and nanocrystalline ceramics were found made by hot-pressing the powders.

Nitrogen doped anatase was investigated (Lin et al 2005) using density functional theory. They have calculated electronic band structures and optical absorption spectra of nitrogen doped anatase. They have found that the optical absorption of nitrogen

doped $TiO_2$ in the visible light region is primarily located between 400 and 500nm. Again nitrogen doped $TiO_2$ has been studied experimentally (Asahi et al 2001) using X-ray photoemission spectroscopy. They have found that nitrogen doped into substitutional sites of $TiO_2$ has proven to be indispensable for band-gap narrowing and photocatalytic activity.

## 1.4 Objectives of the Research

$TiO_2$ anatase is of industrial importance together with rutile. Experimentally it is proven, that anatase is by far more photoactive modification of titanium dioxide compared to rutile. Thus only anatase is used for photo-catalyst. The replacement of either titanium- or oxygen- ions within the crystal lattice will modify the electronic structure.

Doping anatase was the key to open the door to long lasting white pigments in the 1950s. Doping changes the band gap and this will modify the absorption edge of the material. A wider band gap means that only shorter wavelength can be absorbed. Experimentally the doping of $TiO_2$ anatase with platinum and gold enhances its absorption and reflectivity-particularly in nanoclusters.

It has been reported that anatase thin film has different electrical and optical properties from the rutile film (Tang et al 1994a). The essential difference is that anatase thin film appears to have a wider optical absorption gap and a smaller electron effective mass, resulting in a higher mobility for the charge carriers. These properties are beneficial to further applications in optoelectronic and other devices. Therefore it is necessary to have a systematic investigation on the electronic and optical properties of anatase $TiO_2$. Optical properties of $TiO_2$ include a wide electron energy band gap, transparency throughout the visible spectrum, and a high refractive index over a wide spectral range from the ultraviolet to the far infrared. These properties led to the use

of $TiO_2$ for diverse thin film optical and electro-optic device applications (Nakayama et al 1992, Jurek et al 1992). In this work we are going to study the following properties using the planewave pseudopotential DFT methods:

i. Calculate energy cut-off of $TiO_2$ in anatase phase so that we can use it for the determination of the equilibrium structure by means of ab initio method.
ii. Calculate electronic and optical properties of the relaxed structure, and compare them with the experimental values where possible.
iii. We study the effect of varying pressure on electronic and optical properties of anatase $TiO_2$.
iv. Dope anatase $TiO_2$ with precious metal group elements [Platinum (Pt), Gold (Au), Silver (Ag) and Palladium (Pd)] and calculate their electronic and optical properties. These properties will be compared with the experimental or theoretical results where possible.

## 1.5 Outline of the dissertation

This dissertation presents the study of $TiO_2$ anatase phase structure. Electronic, structural and optical properties of anatase have been calculated by using ab initio methods within the Density Functional Theory (DFT).This dissertation consist of four chapters.

In chapter one, we give a general background of anatase and the structural properties. It presents the previous work that have been studied experimentally and other theoretically. It also gives the main applications of our system in some devices and reviews the motivation and objectives of our study. In chapter two, we review the methods that have been employed through our study. Chapter three is all about the

results calculated from our methods and the discussions. We compare our calculated results with the experimental and theoretical results. Chapter four presents the conclusions and recommendation for future work. After chapter four there is a bibliography and finally we have appendix A (list of publications) and appendix B (papers presented at the conferences).

# Chapter 2

# METHODOLOGY

## 2.1 Density Functional Theory

Density functional theory (DFT) is the method used for the quantum mechanical simulation of periodic systems and for the simulation of energy surfaces in molecules. DFT provides accurate structural, energetic and electronic properties not only for solids and surfaces, but also for molecules (Wimmer et al 1987). DFT is based on concepts by Thomas (Thomas 1926) and Fermi (Fermi 1928), who introduced the idea of expressing the total energy of a system as a functional of the total electron density. DFT was developed by Hohenburg and Kohn (Hohenburg et al 1964), and Kohn and Sham (Kohn et al 1965), provided some hope of a simple method for describing the effects of exchange and correlation in an electron gas.

DFT starts with a consideration of the entire electron system. The total energy of a system is expressed as a functional of the total electron density, which in turn depends on the positions of the atoms.

$$E = E[\rho(r), R_\alpha] \tag{2.1}$$

$R_\alpha$ denotes the positions of all atoms $\alpha$ in the system under consideration. In DFT, the total energy is decomposed into three parts: a kinetic energy, an electrostatic or coulomb energy and exchange correlation energy,

$$E_{(\rho)} = T_o + U_{[\rho]} + E_{xc[\rho]}. \tag{2.2}$$

The coulomb energy $U$ is the most straight forward term, which is purely classical and contains the electrostatic energy arising from the coulombic attraction between

electrons and nuclei, the repulsion between all electronic charges, and the repulsion between nuclei

$$U = U_{en} + U_{ee} + U_{nn} \tag{2.3}$$

with

$$U_{en} = -e^2 \sum_{\alpha} Z_{\alpha} \int \frac{\rho(r)}{|r - R_{\alpha}|} dr\,, \tag{2.4}$$

$$U_{ee} = e^2 \iint \frac{\rho(r)\rho(r')}{|r - r'|} dr dr' \tag{2.5}$$

and

$$U = e^2 \sum_{\alpha\alpha'} \frac{Z_{\alpha} Z_{\alpha'}}{|R_{\alpha} - R_{\alpha'}|} \tag{2.6}$$

where *e* is the elementary charge of a proton and $Z_{\alpha}$ is the atomic number of atom α. The Hohenburg-Kohn-Sham theorem, states that the total energy is at its minimum value for the ground state density and that the total energy is stationary with respect to first-order variations in the density, i.e.

$$\frac{\partial E[\rho]}{\partial \rho}\Big|_{\rho=\rho o} = 0.$$

In conjunction with the kinetic energy, one-particle wave functions $\psi i(r)$ is introduced that generate the electron density

$$\rho(r) = \sum_{i} n_i |\psi_i(r)|^2 . \tag{2.7}$$

The set of wave functions that minimize the Kohn-Sham energy functional are given by the self-consistent solutions to the Kohn-Sham equations:

$$\left[-\frac{\hbar^2}{2m}\nabla^2 + V_{ion}(r) + V_H(r) + V_{xc}(r)\right]\psi_i(r) = \varepsilon_i\psi_i(r) \qquad (2.8)$$

where $\psi_i$ is the wave function of the electronic state,

$\varepsilon_i$ is the Kohn-Sham eigenvalue

and $V_H$ is the Hartree potential of the electrons.

$V_H$ is given by

$$V_H(r) = e^2\int\frac{\rho(r')}{|r-r'|}d^3r' \qquad (2.9)$$

and exchange-correlation potential, $V_{xc}$, is given formally by the functional derivative

$$V_{xc}(r) = \frac{\delta E_{xc}[\rho(r)]}{\delta_\rho(r)}. \qquad (2.10)$$

The Kohn-Sham equations must be solved self-consistently so that, the occupied electronic states generate a charge density that produces the electronic potential that was used to construct the equations. Self consistent procedure for solving the kohn-Sham equation is shown in figure2.1. The three terms in the square bracket of figure2.1 represent the kinetic energy of electrons, the coulomb potential due to the all charges in the system, and the exchange-correlation potential.

The Kohn-Sham equations are a set of eigenequations and the terms within the brackets in equation 2.8 can be regarded as a Hamiltonian. Geometry optimization and the self-consistency procedure to solve the Kohn-Sham equations are shown in figure2.2.

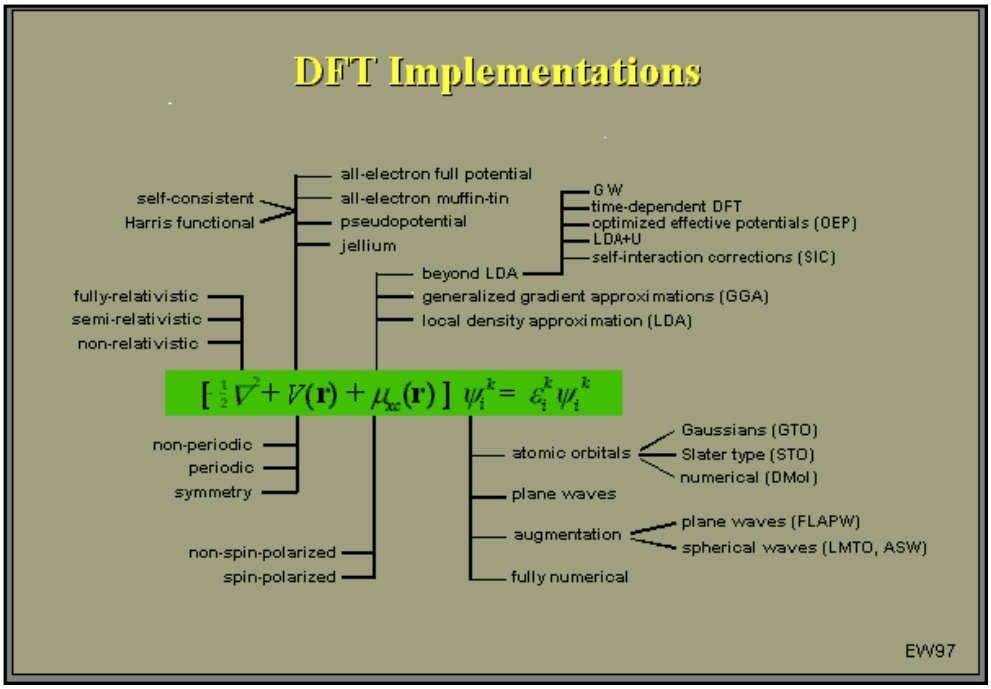


**Figure 2.1: Schematic representative of electronic structure calculations used to solve Kohn-Sham equations (Wimmer 1994).**

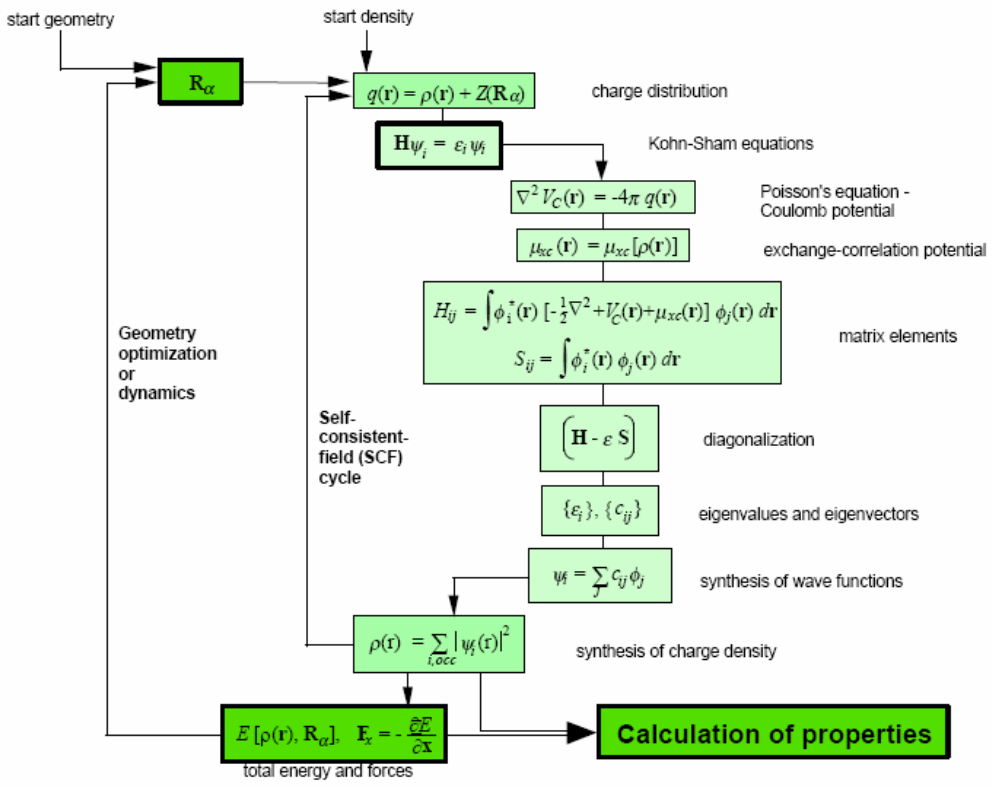


**Figure 2.2: Schematic representation of self-consistency procedure used to solve the Kohn-sham equations and geometry optimization (Freeman et al 1995).**

### 2.1.1 Local Density Approximation

The Kohn-Sham functional described above, must be supplemented by an approximation for the exchange and correlation term. The approximation was proposed by Kohn and Sham which is called local-density approximation (LDA), this approximation is almost universally used in total-energy pseudopotential calculations. In the LDA the exchange-correlation energy of an electronic system is constructed by assuming that the exchange-correlation energy per electron at a point r in the electron gas, $E_{xc}[\rho]$, is equal to the exchange-correlation energy per electron in a homogeneous electron gas that has the same density as the electron gas at point r. Thus

$$E_{xc}[\rho(r)] = \int \varepsilon_{xc}(r)\rho(r)d^3r \tag{2.11}$$

and

$$\frac{\delta E_{xc}[\rho(r)]}{\delta\rho(r)} = \frac{\partial[\rho(r)\varepsilon_{xc}]}{\partial\rho(r)} \tag{2.12}$$

with

$$\varepsilon xc(r) = \varepsilon_{xc}^{\text{hom}}[\rho(r)]. \tag{2.13}$$

LDA has proven that is a good approximation for properties such as structure, bond lengths, vibrational frequencies, elastic moduli and phase stability (of similar structures). LDA describes these properties very reliably for many systems. In principle, the LDA ignores corrections to the exchange-correlation energy at a point r due to nearby inhomogeneities in the electron density. For instance, LDA overestimate the binding energy of many systems and energy barriers in diffusion or chemical reactions may be too small or absent. But LDA is accepted for calculating electronic and structural properties.

### 2.1.2 Generalized Gradient Approximation

The problems seen in LDA can be corrected by the effective potentials that depend on both the local density and the magnitude of its local gradient. This method is called generalized gradient approximation (GGA). It has been reported that GGA overcorrects the local density approximation results but in latter stage the results of GGA agrees well with the results obtained experimentally. In other words GGA goes beyond LDA and it improves the bond lengths of the structure (Perdew et al 1992).

### 2.1.3 Local Spin Density Approximation

LDA has been extended to systems with different densities of spin-up and spin-down electrons. Now the local exchange correlation energy depends on the local electron density and on the local spin density. This approach is called local spin density approximation (LSDA)

## 2.2 Planewave Basis

The many-body problem can be mapped into equivalent observables in an effective single-particle problem. There is a formidable task of handling an infinite number of noninteracting electrons moving in the static potential of an infinite number of nuclei or ions. A wave function must be calculated for each of the infinite number of electrons in the system, and the basis set required to expand each wave function is infinite. Calculations on periodic systems and applying Bloch's theorem to the electronic wave functions can be performed in order to solve the above problems. Bloch's theorem states that in a periodic solid each electron wave function can be written as the product of a cell-periodic part and a wavelike part,

$$\psi_i(r) = \exp[ik.r] f_i(r). \tag{2.14}$$

By using a basis set consisting of a discrete set of plane waves whose wave vectors are reciprocal lattice vectors of the crystal, the cell periodic part of the wave function can be expanded as,

$$f_i(r) = \sum_G c_i, G \exp[iG.r], \tag{2.15}$$

where the reciprocal lattice vectors **G** are defined by **G**.*l*=2π*m* for all *l* where *l* is a lattice vector of the crystal and *m* is an integer. Electron wave function can be written as,

$$\psi_i(r) = \sum_G ci, k+G \exp[i(k+G).r]. \tag{2.16}$$

According to Bloch's theorem, the electron wave functions at each **k** point can be expanded in terms of a discrete plane wave basis set. An infinite plane-wave basis set is required to expand the electronic wave functions. The coefficients $c_{i,\mathbf{k+G}}$ for the plane waves with small kinetic energy $(\hbar/2m)|\mathbf{k}+\mathbf{G}|^2$ are typically more important than those with large kinetic energy. Thus the plane-wave basis set can be truncated to include only plane waves that have kinetic energies less than some particular cutoff energy. Introduction of an energy cutoff to the discrete plane-wave basis set produces finite basis set.

The truncation of the plane-wave basis set at a finite cutoff energy will lead to an error in the computed total energy. However, it is possible to reduce the magnitude of the error by increasing the value of the cutoff energy. The cutoff energy should be increased until the calculated total energy has converged.

When plane waves are used as a basis set for the electronic wave functions, the Kohn-Sham equations assume a particularly simple form. Substitution of equation 2.16 into 2.8 and integration over r gives the secular equation

$$\sum_{G'}\left[\frac{\hbar^2}{2m}\left|k+G\right|^2\delta_{GG'}+V_{ion}(G-G')+V_H(G-G')+V_{XC}(G-G')\right]c_{i,k+G'}=\varepsilon_i c_{i,k+G} \quad (2.17)$$

The kinetic energy is diagonal, and the various potentials are described in terms of their Fourier transforms. Solution of equation 2.17 proceeds by diagonalization of a Hamiltonian matrix whose matrix elements $H_{k+G,k+G'}$ are given by the terms in brackets above. The size of the matrix is determined by the choice of cutoff energy $(\hbar^2/2m)|\ k+G_c|^2$, and will be intractably large for the systems that contain both valence and core electrons.

## 2.3 Pseudopotentials

It has been shown by the use of Bloch's theorem, that a plane wave energy cut-off in the Fourier expansion of the wavefunction and careful *k*-point sampling that the solution to the Kohn-Sham equations for infinite crystalline systems is now tractable. Unfortunately a plane wave basis set is usually very poorly suited to expanding the electronic wavefunctions because a very large number are required to accurately describe the rapidly oscillating wavefunctions of electrons in the core region.

It is well known that most physical properties of solids are dependent on the valence electrons to a much greater degree than that of the tightly bound core electrons. It is for this reason that the pseudopotential approximation is introduced. This approximation uses this fact to remove the core electrons and the strong nuclear potential and replace them with a weaker pseudopotential which acts on a set of pseudo wavefunctions rather than the true valence wavefunctions. In fact, the pseudopotential can be optimised so that, in practice, it is even weaker than the frozen core potential. Schematic diagram of an ionic potentials, valence wave function and the corresponding pseudopotential and pseudo wave function are illustrated in figure

2.3.

The valence wavefunctions oscillate rapidly in the region occupied by the core electrons because of the strong ionic potential. These oscillations maintain the orthogonality between the core and valence electrons. The pseudopotential is constructed in such a way that there are no radial nodes in the pseudo wavefunction in the core region and that the pseudo wavefunctions and pseudopotential are identical to the all electron wavefunction and potential outside a radius cut-off $r_c$. This condition has to be carefully checked for as it is possible for the pseudopotential to introduce new non-physical states (so called *ghost states*) into the calculation. The pseudopotential is constructed, ideally, so that its scattering properties or phase shifts for the pseudo wave functions are identical to the scattering properties of the ion and the core electrons for the valence wave functions, but in such a way that the pseudo wave functions have no radial nodes in the core region. In the core region, the total phase shift produced by the ion and the core electrons will be greater than Л, for each node that the valence functions had in the core region, than the phase shift produces by the ion and the valence band. The phase shift produced by the ion core is different for each angular momentum component of the valence wave function, and so the scattering from the pseudopotential must be angular momentum dependent. The most general form for a pseudopotential is

$$V_{NL} = \sum_{lm} |lm\rangle V_l \langle lm,| \qquad (2.18)$$

where $|lm\rangle$ are the spherical harmonics and $V_l$ is the pseudopotential for angular momentum l.

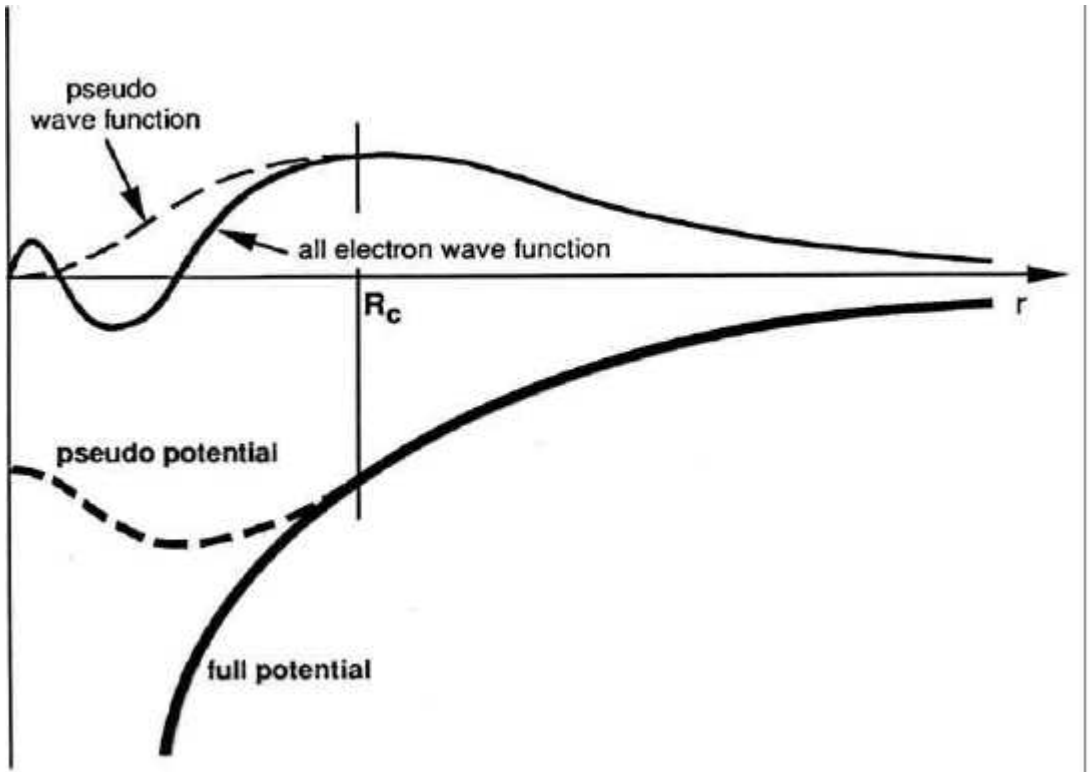


**Figure 2.3: A schematic illustration of all-electron and pseudopotentials and their corresponding wave functions. (Payne et al 1992).**

## 2.4 CASTEP

Cambridge Sequential Total Energy Package (CASTEP) is an ab initio quantum mechanical program employing density functional theory (DFT) to simulate the properties of solids, interfaces, and surfaces for a wide range of materials classes such as ceramics, semiconductors and metals. First principle calculations allow researches to investigate the nature and origin of the electronic, optical and structural properties of a system without the need for any experimental input, with the exception of the atomic number of mass of the constituent atoms. CASTEP uses a total energy plane-wave pseudopotential method. Electronic wavefunctions are expanded through a plane-wave basis set, and exchange and correlation effects in electron-electron interactions can be included within either the local density (LDA) or generalized gradient (GGA) approximations. By combining the use of pseudopotentials and plane wave basis sets makes it extremely easy to calculate the forces on the atoms, enabling efficient optimization of ionic configurations of molecules, solids, surfaces and interfaces.

# Chapter 3
# STRUCTURAL AND ELECTRONIC CALCULATIONS

This chapter presents and discusses the results obtained by the computational methods described in chapter 2, and will be compared with previous experimental and theoretical observations. Section 3.1 presents the structural properties of pure anatase, and section 3.2 the electronic and optical properties. The variations of all these properties with pressure are given in section 3.3. Section 3.4 presents changes associated with doping of anatase with precious metals.

## 3.1 Structure relaxation

### 3.1.1 Energy cut-off

Single energy calculations for pure anatase were performed at different energy cut-offs, within LDA, to establish total energy convergence. $TiO_2$ anatase structure has a large number of atoms; hence we convert the anatase conventional structure to primitive, which is shown in figure 3.1. Figure 3.2 shows a graph of total energy against cut-off.

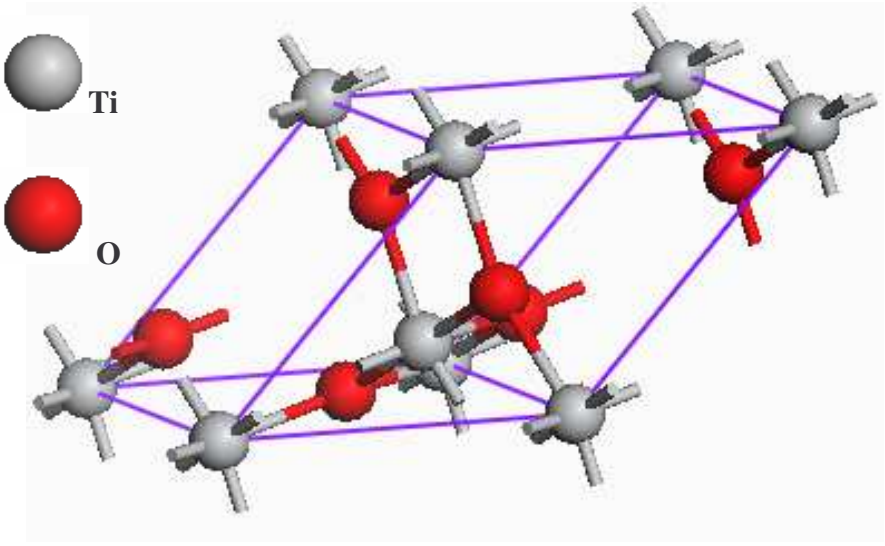


**Figure 3.1: Primitive structure of Titanium dioxide (anatase structure).**

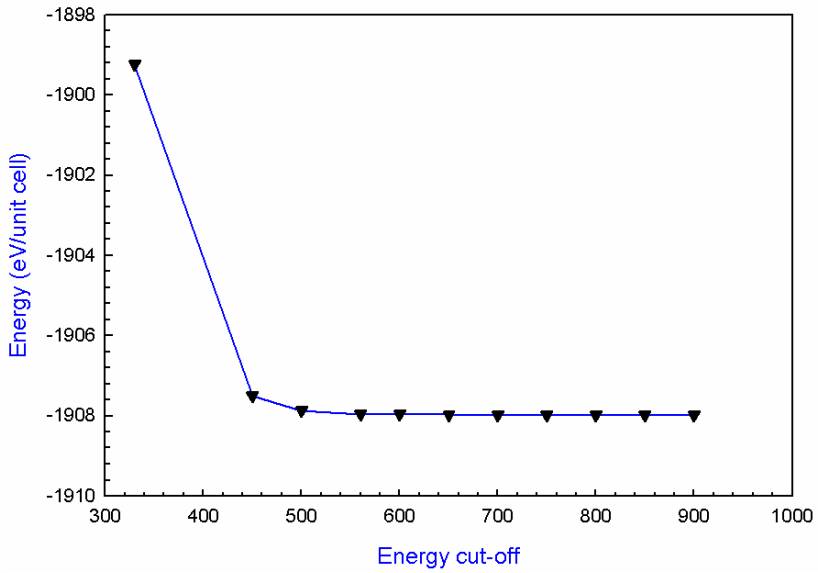


**Figure 3.2: A plot of total energy against cut-off energy for $TiO_2$ in anatase structure.**

The graph shows a steep negative slope from energy cut-off of 350eV to 450eV. From cut-off energy of 500eV it starts to have a slope of zero. So energy cut-off, of 560eV was chosen since at this point total energy stays constant.

### 3.1.2 Geometry optimization

The primitive structure of $TiO_2$ anatase phase was relaxed by performing geometry optimization calculations within LDA and GGA, using energy cut-off of 560eV. The structure was relaxed in order to get optimised lattice parameters. Full geometry optimization anatase system was carried out, which allowed the lattice parameters and coordinates to vary (full geometry optimization). Table 3.1 presents our calculated structural parameters together with experimental (Burdett et al 1987) and other theoretical results (Fahmi et al 1995) obtained using pseudopotential Hartree-Fock (PHF) method. The differences in these structural parameters are very small. Geometric parameters calculated within LDA are close to the experimental and PHF as compared to the ones calculated within GGA, since GGA overcorrects the LDA

results. Both the bond lengths of anatase apical ($d_{ap}$) and equatorial ($d_{eq}$) increase slightly after relaxing the structure.

**Table 3.1: Optimized structural parameters of anatase at cut-off of 560eV compared to experiment (Burdett et al 1987) and the results of PHF calculations (Fahmi et al 1995).**

| | LDA | GGA | PHF | Exp. |
|---|---|---|---|---|
| a (Å) | 3.779 | 3.803 | 3.763 | 3.782 |
| c (Å) | 9.818 | 9.808 | 9.851 | 9.502 |
| c/a | 2.598 | 2.579 | 2.618 | 2.512 |
| $d_{eq}$ | 1.945 | 1.955 | 1.939 | 1.932 |
| $d_{ap}$ | 1.998 | 1.996 | 1.995 | 1.979 |
| Volume ($Å^3$) | 140.2 | 141.8 | 139.5 | 136.2 |

Original and relaxed angles of anatase are presented in table 3.2, where the Ti-O-Ti angle and the smallest O-Ti-O angle (apical) decrease by small amounts. The largest O-Ti-O angle (equatorial) increases slightly.

**Table 3.2: Original and relaxed angles of $TiO_2$ anatase phase.**

| Bond angle | Original angle | Relaxed angle |
|---|---|---|
| Ti-O-Ti | 156.2 | 153.1 |
| O-Ti-O (apical) | 78.1 | 76.5 |
| O-Ti-O (equatorial) | 101.9 | 103.5 |

The atomic positions for the unrelaxed and optimized structures of anatase are shown in tables 3.3 and 3.4 respectively. Optimized atomic positions from GGA and LDA are close to each other, hence only atomic positions obtained from LDA are shown. There is no change in the positions of the titanium atoms and for oxygen atoms; there is a small change after three significant figures for oxygen atoms only.

**Table 3.3: Original atomic positions of titanium dioxide in anatase phase.**

| | x | y | z |
|---|---|---|---|
| Ti1 | 0.0 | 0.0 | 0.0 |
| Ti2 | 0.75 | 0.25 | 0.5 |
| O1 | 0.20338 | 0.20338 | 0.0 |
| O2 | 0.95338 | 0.45338 | 0.5 |
| O3 | 0.54662 | 0.04662 | 0.5 |
| O4 | -0.20338 | -0.20338 | 0.0 |

**Table 3.4: Optimized atomic positions of titanium dioxide in anatase phase.**

| | x | y | z |
|---|---|---|---|
| Ti1 | 0.0 | 0.0 | 0.0 |
| Ti2 | 0.75 | 0.25 | 0.5 |
| O1 | 0.20346 | 0.20346 | 0.0 |
| O2 | 0.95346 | 0.45346 | 0.5 |
| O3 | 0.54654 | 0.04654 | 0.5 |
| O4 | -0.20346 | -0.20346 | 0.0 |

## 3.2 Electronic and optical properties of $TiO_2$

In this section we present and discuss the calculated electronic properties of anatase which include density of states (DOS), charge density and charge differences. We used DOS integrated method of smearing, with the smearing width of 0.2eV to plot the DOS of $TiO_2$. The density of states analysis are in general instructive in understanding the bonding nature of a compound, furthermore the band-gap assists in classifying the system as either an insulator, semiconductor or metallic. We also present the optical properties of anatase, particularly the dielectric function (real and imaginary parts), energy loss function, absorption edge and reflectivity, all as a function of energy.

### 3.2.1 Density of states

Figure 3.3 shows the total and partial densities of states for pure anatase structure. The DOS were calculated using plane wave pseudo potential method (Payne et al 1992). The bottom panel is the partial DOS for oxygen (O), the middle panel is for titanium (Ti) and the upper panel is the total DOS for $TiO_2$. The valence band (VB) and the conduction band (CD) of the total DOS form three groups of states neatly separated by gaps. The peak at about -16eV is predominantly from $O_{2s}$ with the minor presence of $Ti_{3d}$. The last peak in the valence band extending from -5 to 0eV emanates from $O_{2p}$ and a smaller $Ti_{3d}$, which shows a strong hybridization between $O_{2p}$ and $Ti_{3d}$. The first peak in the conduction band ranging from 0.0 to 6.0eV is dominantly of $Ti_{3d}$ with a small contribution of $O_{2p}$ yielding some Ti-O anti-bonding. The Fermi level lies at the top of the valence band and a band gap of 2.2eV was observed indicating that anatase is an insulator. Our value is much smaller than the experimental value of 3.2eV (Tang et al 1993), and it is well known that the DFT values of the energy band gap value is normally not comparable to the experimental values.

### 3.2.2 Charge density

In order to describe the bonding natural for $TiO_2$, we have calculated the electronic charge density and electronic charge difference using plane wave pseudopotential method. Figure 3.4 presents charge density difference for the (110) plane of $TiO_2$. Colours indicate the loss (blue) and the gain (red) of charge. Charge density difference shows that oxygen has gained charge and titanium has suffered loss of some charge. Ti and O atoms show that charge density differences are directional, and there is a strong bonding between Ti-O than in Ti-Ti and O-O bond. Figure 3.5 presents electron charge density of anatase in the (110) plane and higher charge

density around O-atoms than in Ti-atoms is noted.

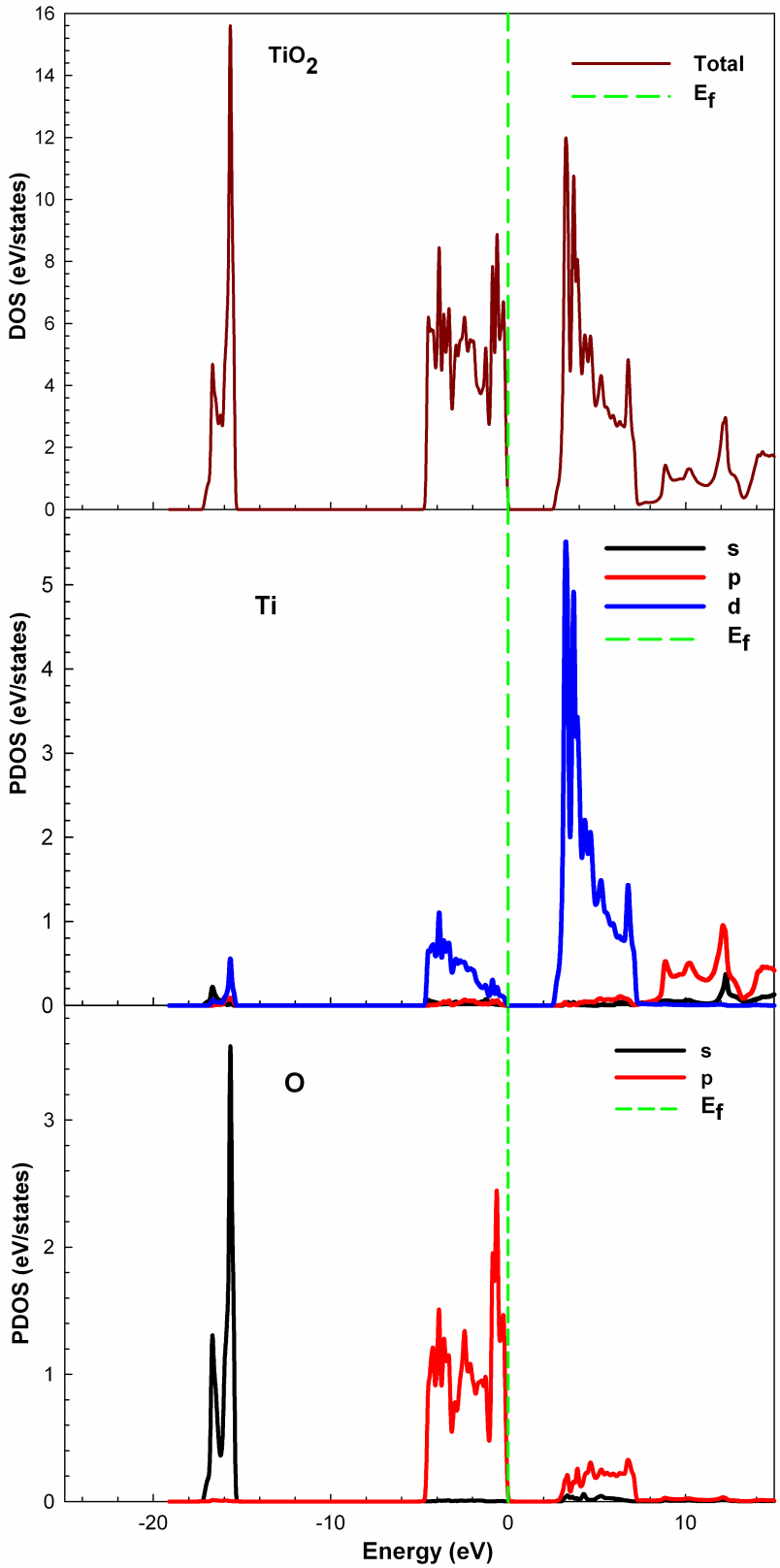


**Figure 3.3: Total and partial DOS for $TiO_2$ anatase structure. The Fermi energy is taken as the energy zero ($E-E_f=0$).**

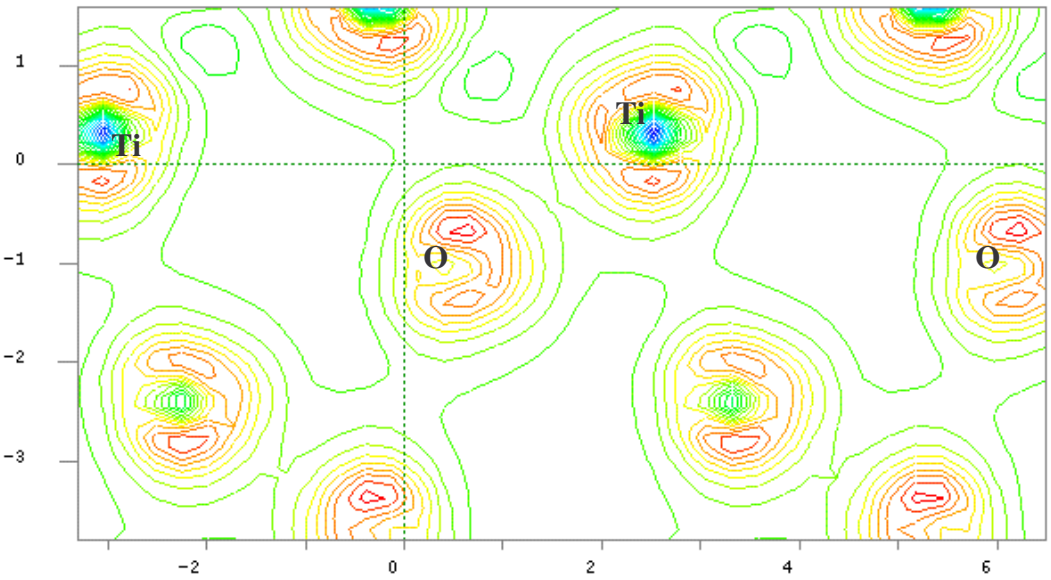


**Figure 3.4: Charge density difference of $TiO_2$ anatase in the (110) plane.**

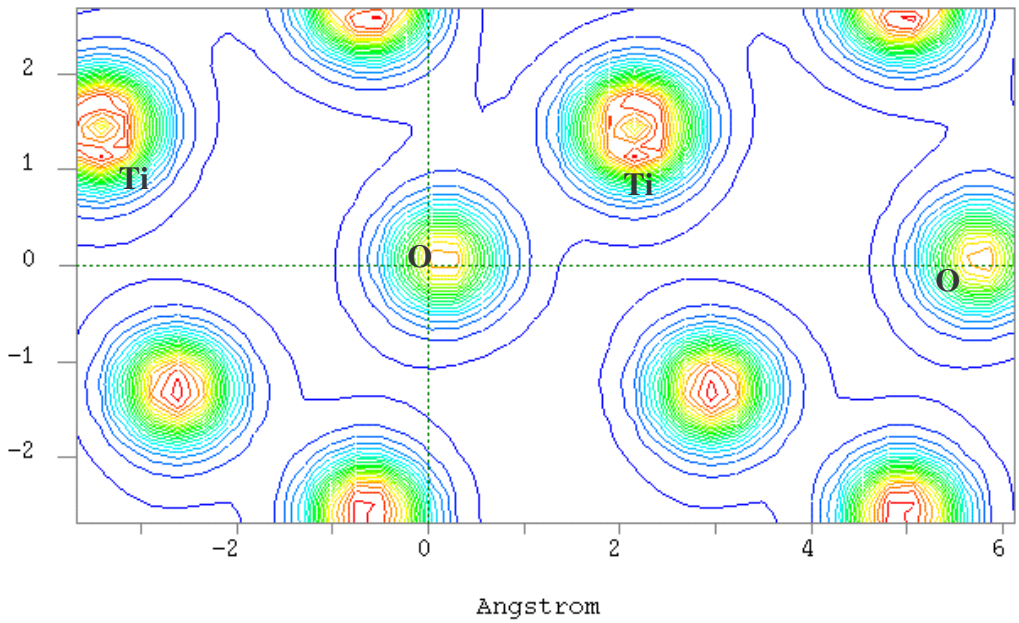


**Figure 3.5: Electron charge density of $TiO_2$ anatase in (110) plane.**

### 3.2.3 Optical properties

In this section we present the optical properties of anatase structure. Calculations have been computed at optical volume using plane-waves pseudopotential method. In practice, the behaviour of materials can be described by a complex refractive index, N, which is given by

$$N = n + ik . \tag{3.1}$$

In vacuum N is real, and equal to unity. For transparent materials it is purely real, the imaginary part being related to the absorption coefficient by,

$$\eta = \frac{2\kappa\omega}{c} . \tag{3.2}$$

This absorption coefficient indicates the fraction of energy lost by the wave when it passes through a unit thickness of the material. It is derived by considering the rate of production of Joule heat in the sample. The reflection coefficient can be obtained for the simple case of normal incidence onto a plane surface by matching both the electric and magnetic fields at the surface, which is given by

$$R = \left|\frac{1-N}{1+N}\right|^2 = \frac{(n-1)^2 + k^2}{(n+1)^2 + k^2} . \tag{3.3}$$

However, when performing calculations of optical properties it is common to evaluate the complex dielectric constant and then express other properties in terms of it. The complex dielectric constant, ε ($\omega$), is given by

$$\varepsilon = \varepsilon_1 + \imath\varepsilon_2 = N^2 , \tag{3.4}$$

and hence the relation between the real and imaginary parts of the refractive index and dielectric constant is

$$\varepsilon_1 = n^2 - k^2 , \varepsilon_2 = 2nk . \tag{3.5}$$

Another frequently used quantity for expressing optical properties is the optical

conductivity, σ ($\omega$)

$$\sigma = \sigma_1 + i\sigma_2 = -i\frac{\omega}{4\pi}(\varepsilon - 1). \tag{3.6}$$

Optical conductivity is usually used to characterize metals; however CASTEP is aimed more towards the optical properties of insulators and semiconductors. The main difference between the two is that intraband transitions play important role in the IR part of the optical spectra of metals and these transitions are not considered at all in CASTEP.

A further property that can be calculated from the complex dielectric constant is the energy loss function. It describes the energy lost by an electron passing through a homogeneous dielectric material and is given by

$$\mathrm{Im}\left(\frac{-1}{\varepsilon(\omega)}\right). \tag{3.7}$$

The imaginary part of the dielectric constant is given by

$$\varepsilon_2\left(q - O_{\hat{u},\hbar\omega}\right) = \frac{2e^2\pi}{\Omega\varepsilon_o}\sum_{k,v,c}\left|\left\langle \Psi_k^c \left| \hat{u}.r \right| \Psi_k^v \right\rangle\right| 2\delta\left(E_k^c - E_k^v - E\right), \tag{3.8}$$

where u is the vector defining the polarization of the incident electric field. This expression is similar to Fermi's Golden rule for time dependent perturbations, and $\varepsilon_2(\omega)$ can be thought of as detailing the real transitions between occupied and unoccupied electronic states. Since the dielectric constant describes a causal response, the real and imaginary parts are linked by a Kramers-Kronig transform. This transform is used to obtain the real part of the dielectric function, $\varepsilon_1(\omega)$. The value of $\varepsilon_1(\omega)$ is the most important information in the limit of zero frequency.

To get optical properties of $TiO_2$ we firstly calculated matrix elements and dielectric function with light unpolarized, which produces optical properties in the plane perpendicular to the incident direction. Unpolarized: requires a vector to define the

direction of propagation of incident light at normal incidence to the crystal.

The calculated real part and imaginary part of the dielectric function for the anatase up to energy of 12eV are shown in figure 3.6 and are compared with the results found using the first-principles orthogonalized linear-combinations-of-atomic-orbitals (OLCAO) (Mo et al 1995). We observe a very good agreement between the OLCAO and calculated imaginary part of the dielectric constant. The calculated imaginary dielectric constant shows one broad peak ranging from 4eV to 5eV, and a small peak ranging from 7eV to 8eV, which is similar to the OLCAO results. At approximately 6eV the dielectric constant curves drops for both cases, however the OLCAO values reduce more significantly than the calculated. The calculated real dielectric constant has a peak at 3.2eV, which agrees reasonably with the OLCAO results and is higher than the latter by less than 5%. The OLCAO real dielectric constant decreases drastically at about 5.5eV than the calculated spectrum.

We have calculated the optical transition of anatase up to higher photon energy of 20eV, in order to analyze energy loss function. Figure 3.7 shows the calculated and OLCAO energy loss functions as a function of energy for anatase. An aggregate of peaks is noted between 11eV and 19.8eV for both the calculated and OLCAO results. The first OLCAO plasma peak occurs at 12.7eV, which is close to our calculated peak at about 11eV. The OLCAO peak has a higher energy loss function of 1.8 while the value of its calculated counterpart is 1.21.

Figure 3.8 and 3.9 show the absorption and reflectivity curves for anatase respectively as a function of energy. The absorption edge of anatase was calculated up to 4eV and the reflectivity up to energy of 12eV with light unpolarized. The calculated absorption edge commences at 1.2eV, while the experimental absorption edge starts at 3.2eV. Calculations of reflectivity have been carried out up to 11eV and distinct peaks are

noted at 4.7eV and 8.8eV. Experimental measurements (Tang et al 1994b) were terminated at 5.9eV, and a reflectivity peak at 4.3eV corresponds reasonably with our calculated results.

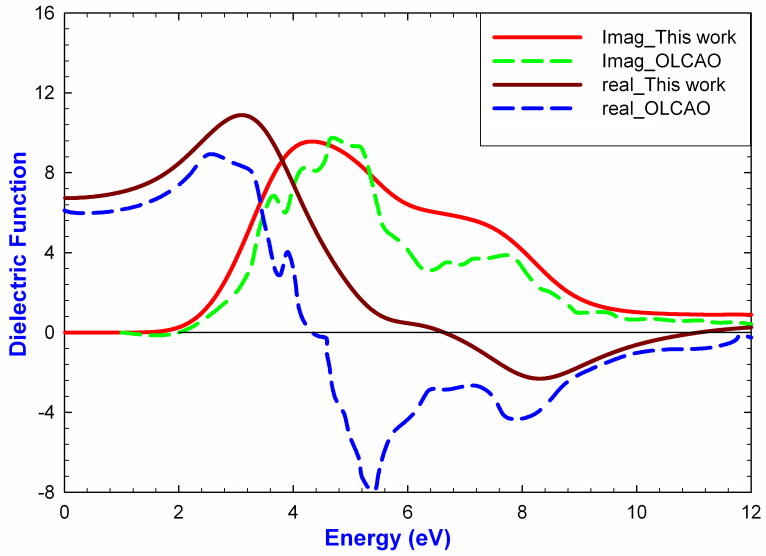


**Figure 3.6: Calculated and OLCAO (Mo et al 1995) real parts and imaginary parts of the dielectric functions of anatase.**

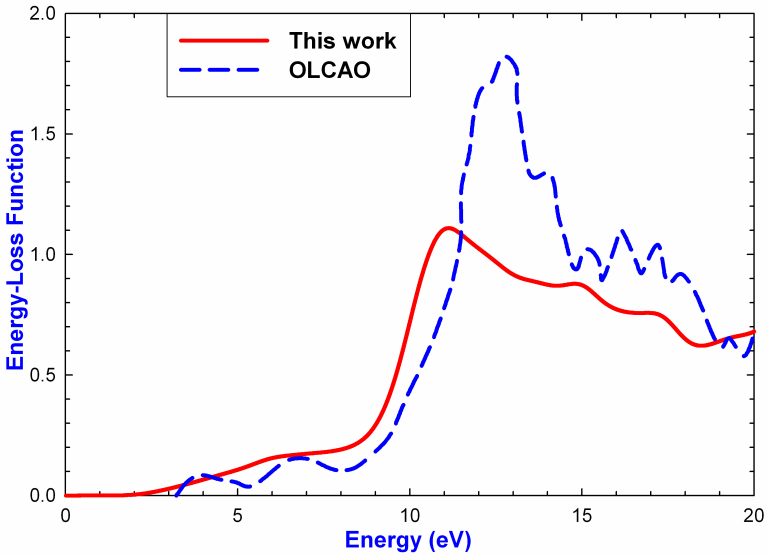


**Figure 3.7: Calculated and OLCAO (Mo et al 1995) energy-loss functions for anatase.**

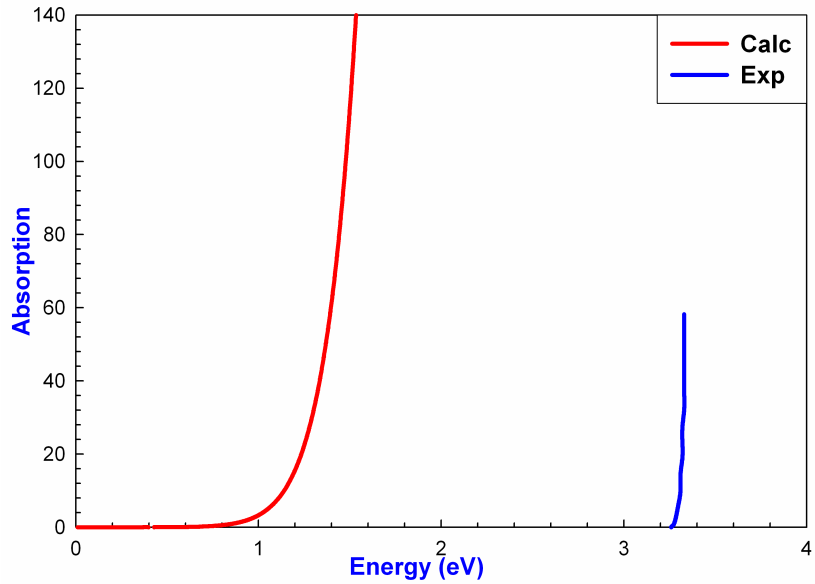


**Figure 3.8: Absorption edges of anatase calculated and experimental (Tang et al 1994b).**

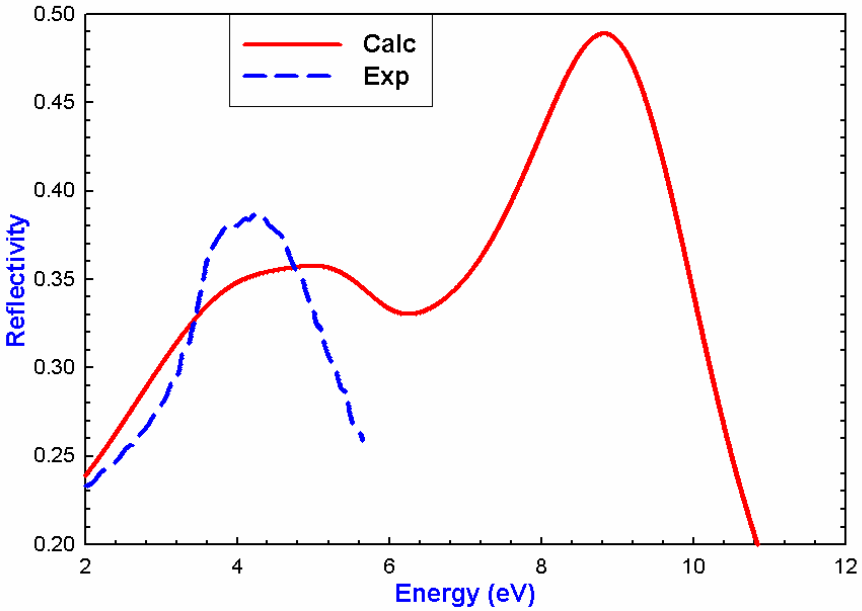


**Figure 3.9: Calculated and experimental (Tang et al 1994b) reflectance spectra of anatase.**

We have further calculated absorption and reflectivity as a function of wavelength (nm), in order to study optical properties in the visible region; that is between 400nm and 500nm. In figure 3.8 and 3.9 we have absorption and reflectivity as a function of

energy (eV), hence we converted energy (eV) of the experiments (Tang et al 1994b) to wavelength (nm) by using energy conversion calculator from (http://www.ilpi.com/msds/ref/energyunits.html). Figure 3.10 compares calculated and experimental absorption spectra of anatase as a function of wavelength and they accord well in the visible region. Absorption spectrum of the experiment ranges up to 550nm while our calculated spectrum terminates at 800 nm. At higher wavelength that is after visible region both absorption spectra reach zero absorption or equilibrium absorption. Figure 3.11 shows calculated and the experimental reflectance spectra of anatase as a function of wavelength. Experimental reflectivity was measured up to 620nm and our calculated reflectivity ranges to 800nm. A broad peak is predicted at smaller wavelength in agreement with experimental results, although the latter peak is shifted to the right. Beyond the visible region both the calculated and experimental reflectivities show a slight decrease, which ultimately tend to a constant value. In general there is a good correlation between our calculated and the experimental absorption and reflectivity.

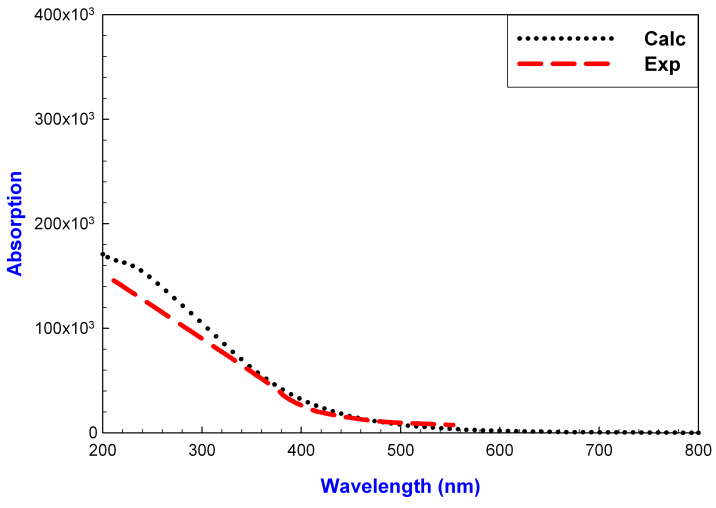


**Figure 3.10: Calculated and experimental (Tang et al 1994b) absorption spectra of anatase against wavelength.**

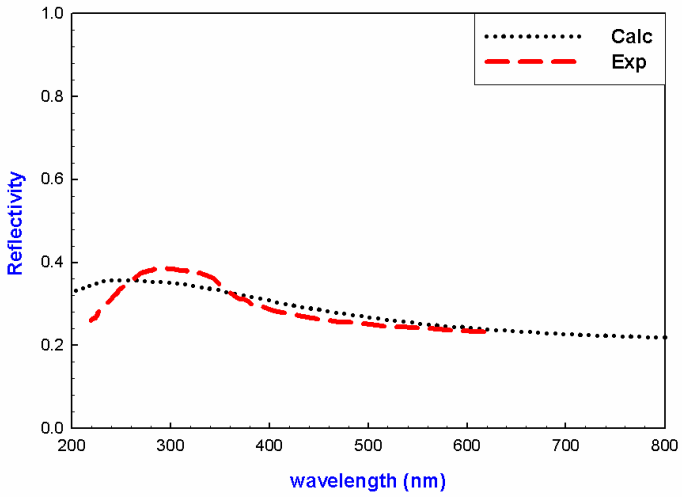


**Figure 3.11: Calculated and experimental (Tang et al 1994b) reflectance spectra of anatase against wavelength.**

## 3.3 Pressure dependence on parameters, properties and equation of state.

### 3.3.1 Pressure dependence on parameters

By using the CASTEP code with the method described in chapter 2 we have calculated the volume of anatase as a function of pressure. Structural parameters of anatase unit cell at zero pressure are presented in table 3.5. Our calculated parameters at zero pressure agree well with the experimental (Swamy et al 2001a, Horn et al 1972, Howard et al 1991.) with the percentage deviation of less than 5%. Our results also agree well with the calculations using PS-HF method (Fahmi et al 1995). Calculations were carried out for various pressures ranging from 0 to 7.8GPa. Table 3.6 presents the results of unit cell and volume of anatase as a function of pressure.

**Table 3.5 Structural data for anatase $TiO_2$ at zero pressure and lengths in Å. The dashed lines indicate that no values were attained.**

| | a (Å) | c (Å) | c/a | $d_{ap}$ | $d_{eq}$ |
|---|---|---|---|---|---|
| Calc (This work) | 3.803 | 9.806 | 2.578 | 1.997 | 1.955 |
| Calc (Fahmi et al 1995) | 3.763 | 9.851 | 2.618 | 1.995 | 1.939 |
| Exp (Swamy et al 2001a) | 3.791 | 9.515 | 2.510 | ----- | ------ |
| Exp (Horn et al 1972) | 3.784 | 9.515 | 2.515 | 1.980 | 1.934 |
| Exp (Howard et al 1991) | 3.785 | 9.514 | 2.513 | 1.978 | 1.934 |

We have plotted ratio of the lattice parameters to the equilibrium zero- pressure values of the unit-cell lattice constants against pressure and the ratio c/a against V/Vo. This was done in order to study the behaviour of our system parameters under different pressures and compare them with the experimental results. A plot of ratio ($a/a_o$) against pressure (fig. 3.12) shows that if the pressure increases the ratio decreases for both calculated and experiment. Our ratio ($a/a_o$) is more than the experimental ratio ($a/a_o$).

**Table 3.6: Pressure dependence of the structural parameters of anatase.**

| Pressure (GPa) | a (Å) | c (Å) | V ($Å^3$) | $V/V_o$ | $c/c_o$ | $a/a_o$ | c/a |
|---|---|---|---|---|---|---|---|
| 0.0 | 3.803 | 9.806 | 141.798 | 1 | 1 | 1 | 2.510 |
| 2.0 | 3.801 | 9.692 | 140.066 | 0.988 | 0.995 | 0.997 | 2.503 |
| 2.7 | 3.803 | 9.642 | 139.487 | 0.984 | 0.992 | 0.996 | 2.500 |
| 3.9 | 3.801 | 9.597 | 138.641 | 0.978 | 0.989 | 0.995 | 2.497 |
| 5.3 | 3.799 | 9.523 | 137.502 | 0.970 | 0.986 | 0.993 | 2.492 |
| 6.5 | 3.795 | 9.501 | 136.832 | 0.965 | 0.983 | 0.991 | 2.488 |
| 7.8 | 3.788 | 9.486 | 136.133 | 0.960 | 0.980 | 0.990 | 2.483 |

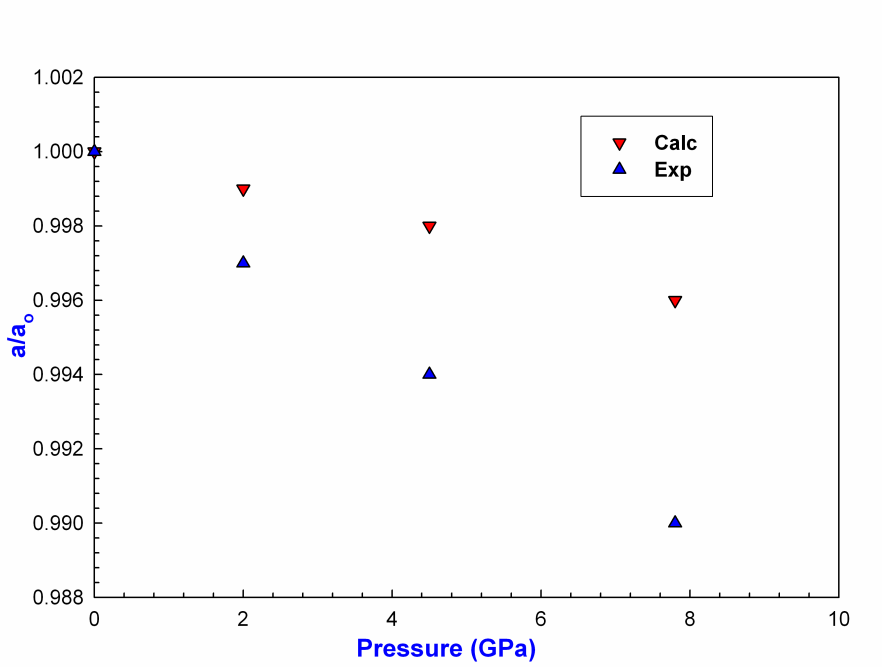


**Figure 3.12: Relative parameter $a/a_o$ as a function of pressure for anatase.**

Figure 3.13 presents the calculated and experimental (Swamy et al 2001a) plots of the ratio ($c/c_o$) against pressure (GPa), which shows that the increase in pressure decreases the ratio ($c/c_o$) in a similar way to the graph of ratio ($a/a_o$) against pressure.

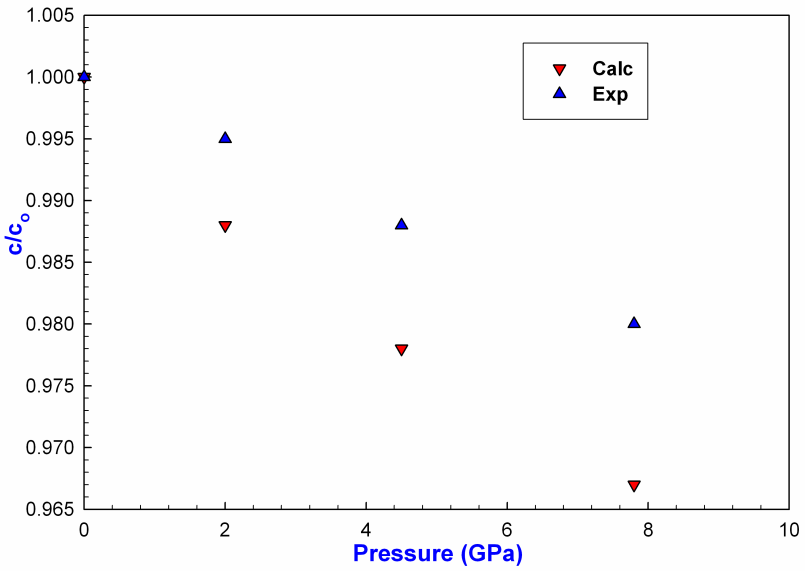


**Figure 3.13: Relative parameter $c/c_o$ as a function of pressure for anatase.**

In order to understand the compressibility of our system we consider the ratio (c/a) against pressure and the relative volume ($V/V_o$). The plots of calculated c/a against pressure and relative volume are shown in figure 3.14 and 3.15 respectively, together with the experimental results. There is a reasonable agreement in trends between our calculated and the experimental results. Our calculated results slightly underestimate the compressibility of our system.

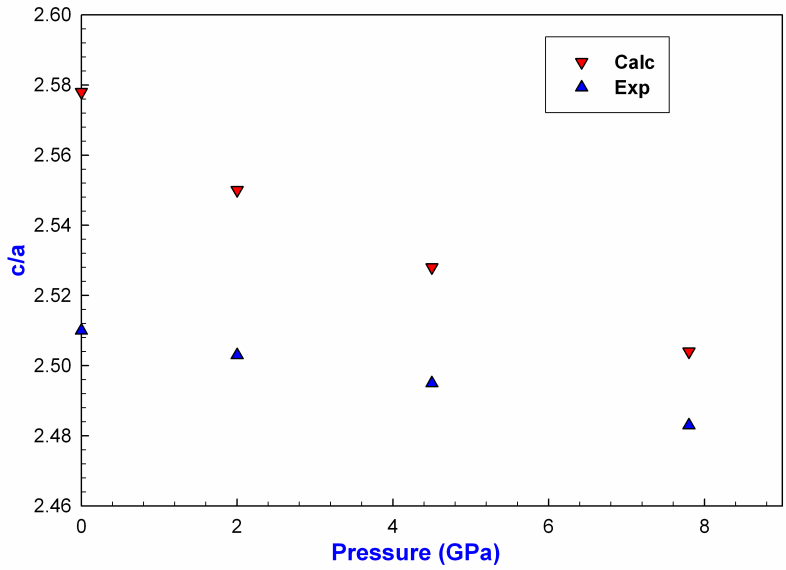


**Figure 3.14: Lattice parameter c/a as a function of pressure for anatase.**

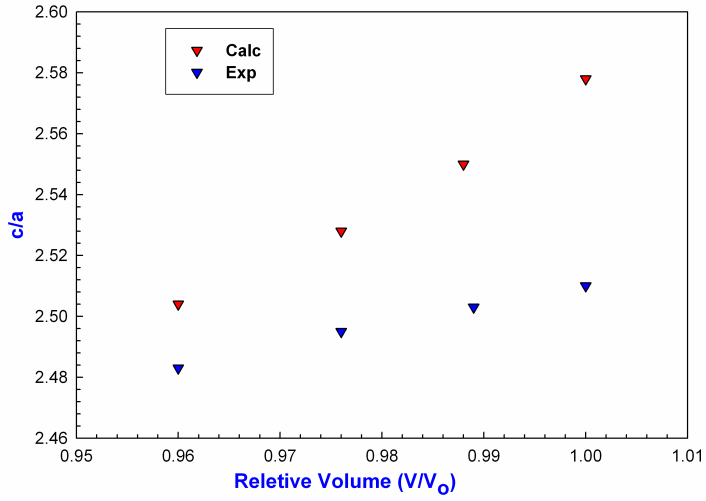


**Figure 3.15: Lattice parameter c/a as a function of relative volume ($V/V_o$) for anatase.**

Figure 3.16 and 3.17 present graph of equatorial and apical Ti-O bond distances respectively, where they show clearly the compressibility of anatase. As the pressure increases both Ti-O bonds decrease. This compressibility of our system agrees reasonably with the results carried out with the all-electron linear combination of atomic orbitals (LCAO) (Muscat et al 2002).

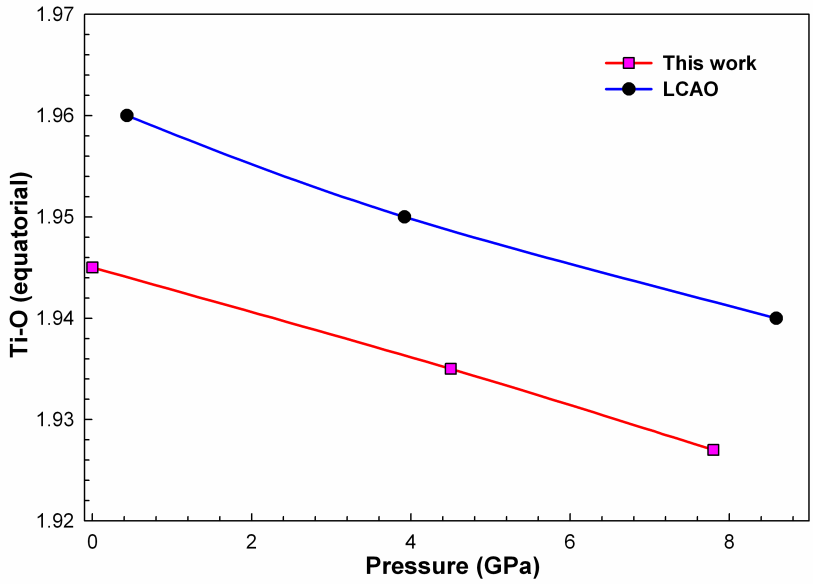


**Figure 3.16: Plot of equatorial (Ti-O) against pressure of anatase.**

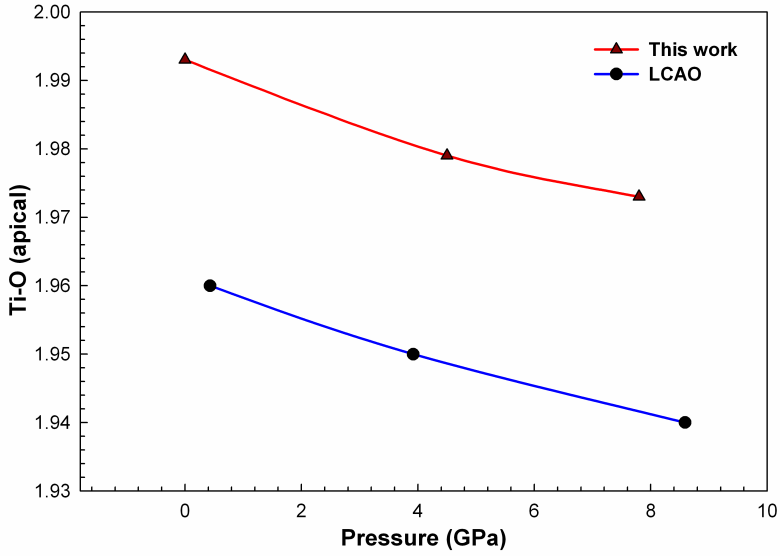


**Figure 3.17: Plot of apical (Ti-O) against pressure of anatase.**

### 3.3.2 EOS Bulk Modulus

We have deduced the bulk modulus (B) of anatase from graph on figure 3.18, by fitting to the third order Birch- Murnaghan equation (Murnaghan 1944). Reasonable model would be with a constant bulk modulus

$$B = -V\left(\frac{\partial P}{\partial V}\right)_T$$

Our bulk modulus was found to be 178.9GPa which agrees well with the experimental value (Arlt et al 2000) of 179GPa. The experimental value was found by using polycrystalline as well as single-crystal material.

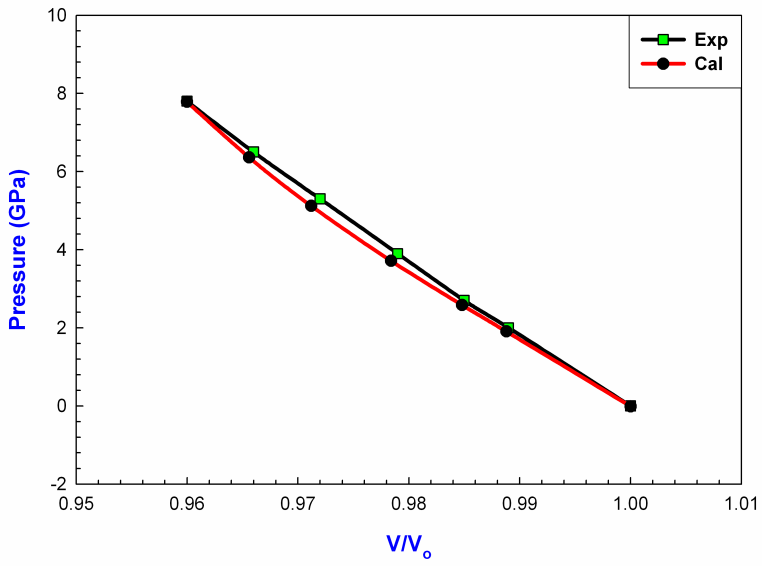


**Figure 3.18: Calculated and experimental (Swamy et al 2001a) plot of pressure against V/Vo for the bulk modulus of anatase.**

The value of bulk modulus of anatase obtained experimentally (Swamy et al 2001a) using X-ray diffraction measurements in a diamond anvil cell is 178±1GPa, which is in good agreement with our calculated value of 179GPa. We present three different experimental results of anatase in table 3.7 and compare them with our calculated value. From table 3.7 we note that two of the experimental bulk moduli (a and b) are

close or similar to our calculated bulk modulus. The third experimental (Lagarec et al 1995) bulk modulus is twice as much as our calculated and differs from other experimental values. The other bulk modulus which is obtained by using Morse stretch (M-Q) interatomic is 176GPa (Swamy et al 2001b), this value is close to our calculated bulk modules. Calculated and experimental (Swamy et al 2001a) plots of unit cell volume against pressure are shown in figure 3.19, clearly indicating a good correlation on how the volume reduces with pressure.

**Table 3.7: Calculated and experimental values of bulk modulus.**

| | B (GPa) |
|---|---|
| Calc. | 178.9 |
| Exp.[a] | 179.0 |
| Exp.[b] | 178.0 |
| Exp.[c] | 360.0 |
| Exp.[d] | 176.0 |

[a] (Arlt et al 2000)

[b] (Swamy et al 2001a)

[c] (Lagarec et al 1995)

[d] (Swamy et al 2001b)

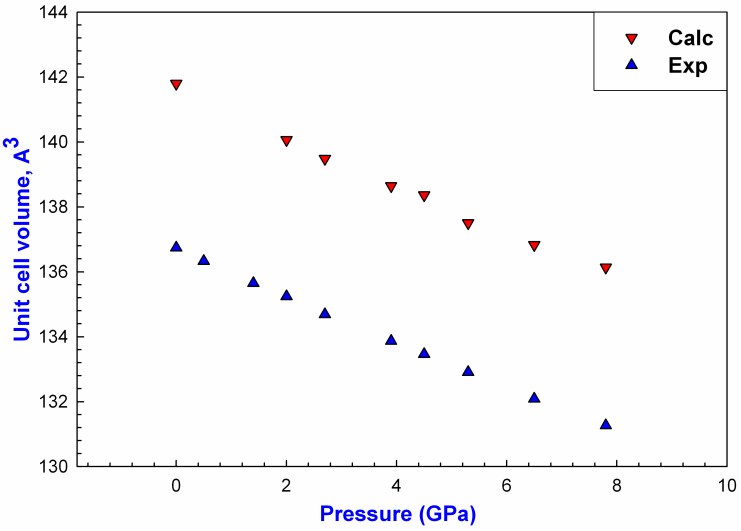


**Figure 3.19: Plot of unit cell volume against pressure of anatase.**

### 3.3.3 The influence of pressure on the optical spectra

We have calculated the reflectivity, absorption, real part dielectric function, imaginary dielectric function and loss function for anatase at different pressures. For unpolarized light our properties are perpendicular to the incident direction. Absorption spectra of anatase as a function of frequency is shown in figure 3.20. At lower frequency ranging below 35eV, the absorption spectrum show predominant higher peaks at 6 and 28eV at higher pressure (12GPa). The absorption shows changes from 25eV and reduces drastically to zero at higher frequency above 35eV when the pressure is increased from 7.8 to 12GPa. Figure 3.21 presents absorption spectra of anatase against wavelength at different pressures. The absorption increases as the pressure is increased at lower wavelengths and decreases with pressure at higher wavelengths above 250nm. Beyond 500nm, spectra related to different pressures overlap until they reach absorption of zero. Figure 3.22 presents the reflective spectra of anatase as a function of wavelength at different pressures. The reflectivity increases with pressure at lower wavelength below 300nm and decreases at higher wavelength above 300nm. Such enhancements and reductions in the reflectivity are slight from 0 to 7.8GPa and clearly distinguishable at 12GPa. Figures 3.23 and 3.24 present real and imaginary parts of the dielectric constant respectively at different pressures. We note that there is not much difference for the real and imaginary parts as the pressure is varied. Figure 3.25 presents the loss function of $TiO_2$ at different pressures. The spectra in the pressure range from 0 to 7.8GPa show similar features, with those of 4.5 and 7.8 almost coincident. However at 12GPa, the loss function is generally higher than at lower pressures and it crosses over to lower values at 34eV. In general, changes in the optical properties of anatase are noted at 12GPa.

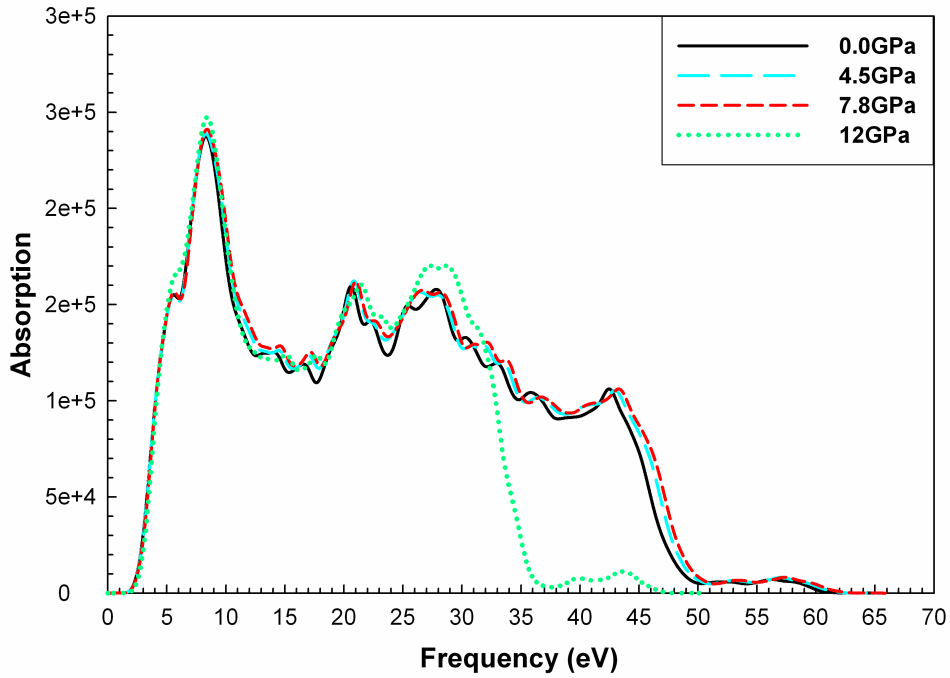


**Figure 3.20: Absorption spectra of $TiO_2$ as a function of frequency at different pressures.**

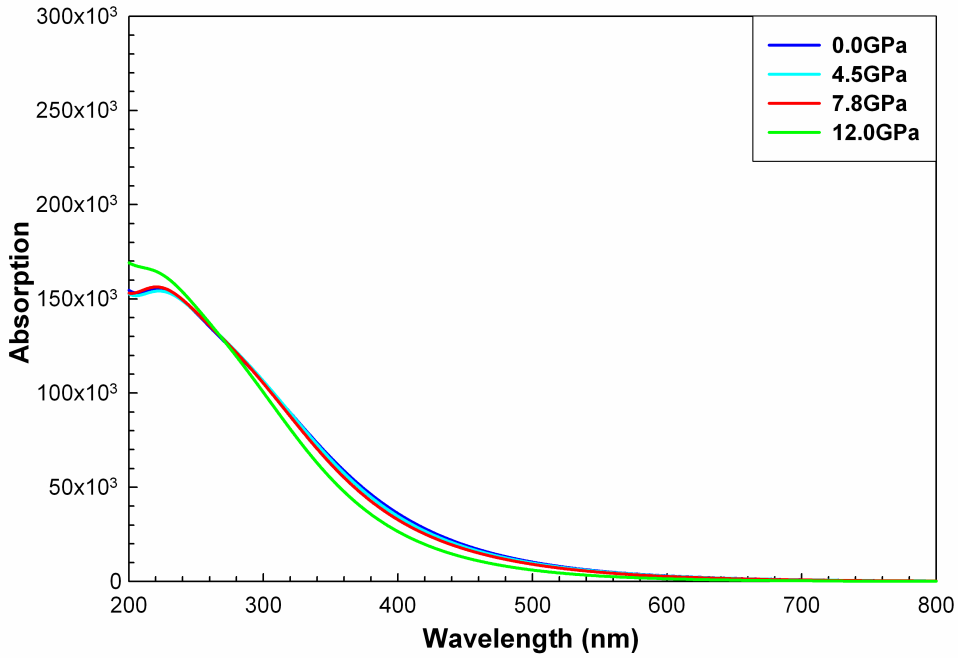


**Figure 3.21: Absorption spectra of $TiO_2$ as a function of wavelength at different pressures.**

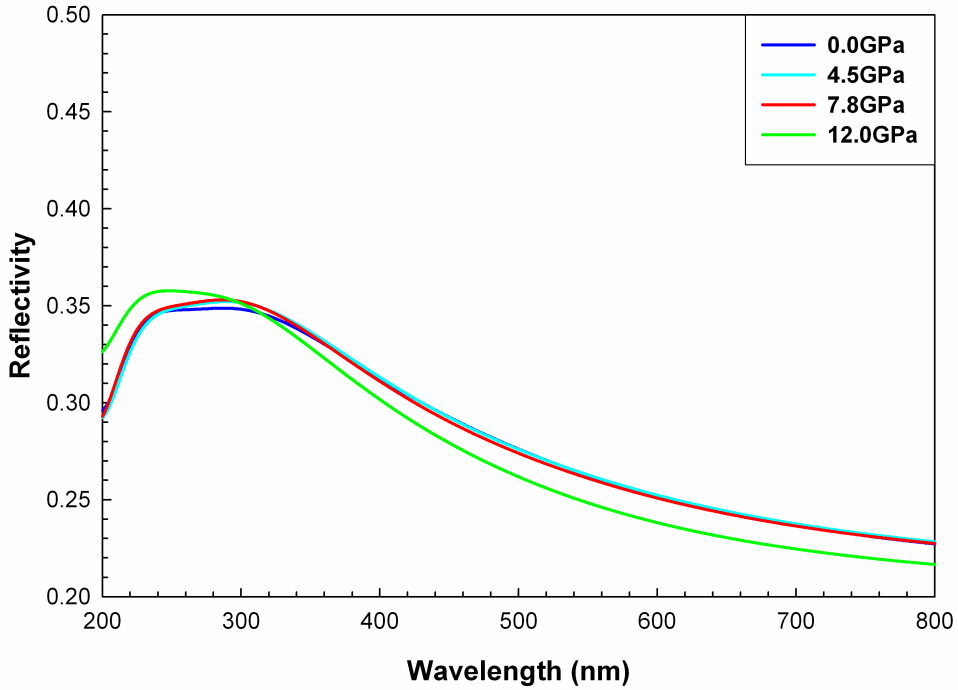


**Figure 3.22: Reflectivity spectra of $TiO_2$ as a function of wavelength at different pressure.**

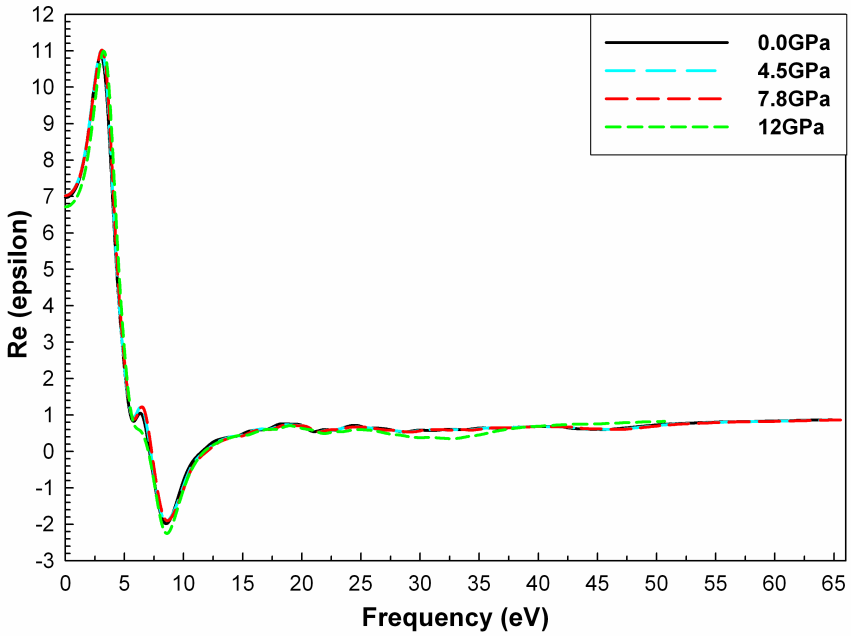


**Figure 3.23: Calculated real parts of the dielectric constant for $TiO_2$ at different pressures.**

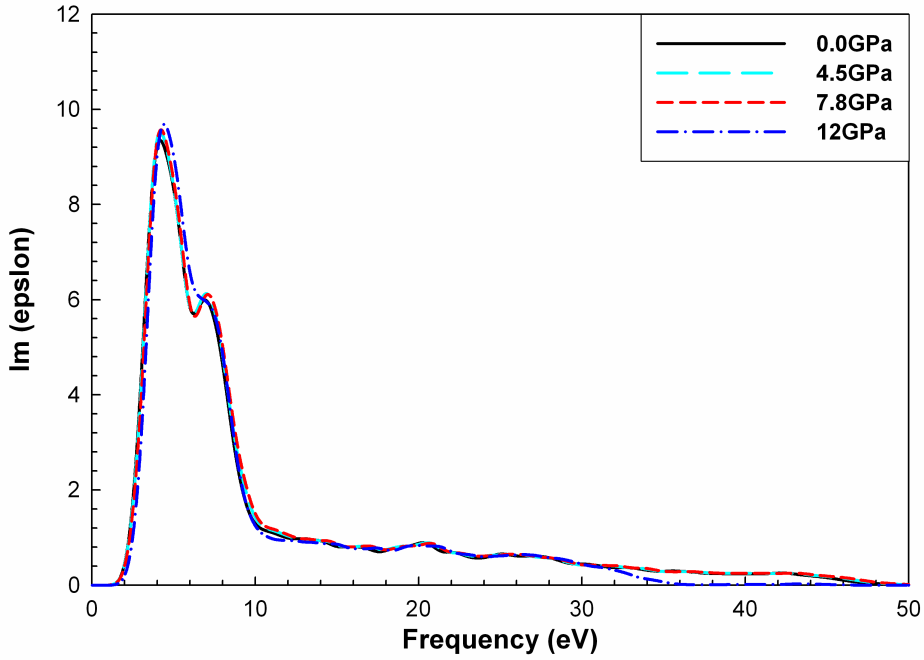


**Figure 3.24: Calculated imaginary parts of dielectric constant for $TiO_2$ at different pressure.**

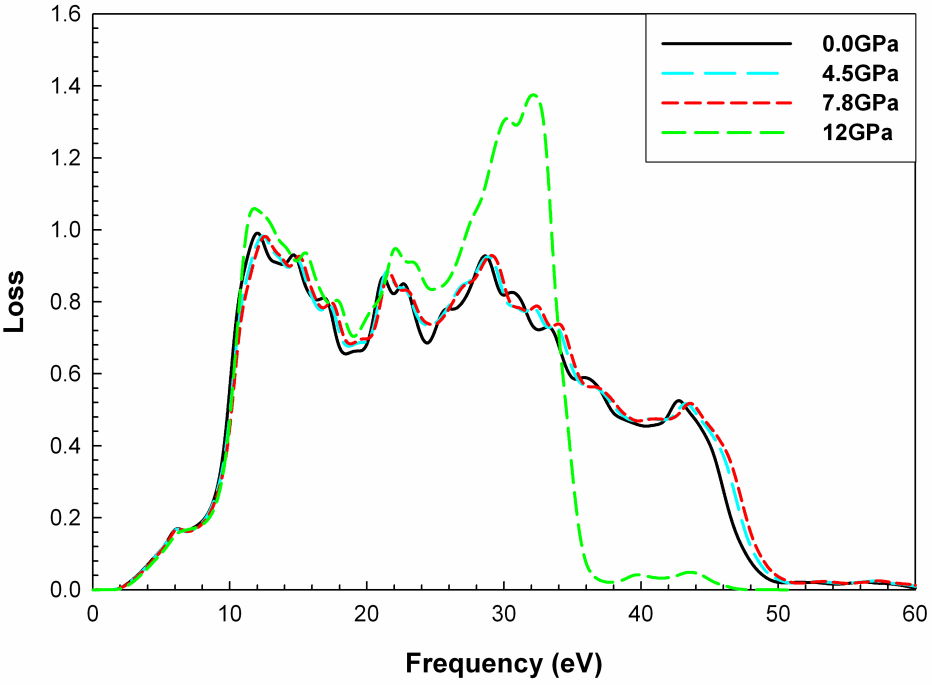


**Figure 3.25: Calculated loss function of $TiO_2$ at different pressure.**

## 3.4 Precious metals doped $TiO_2$

This section presents the results of transition metals doped anatase, with the precious metals platinum (Pt), gold (Au), silver (Ag) and palladium (Pd). We study their optical and electronic properties, and compare them with the pure anatase. It also presents properties associated with doping interstitially and by substitution.

### 3.4.1 Optical properties

We have calculated structural parameters of interstitially doped anatase with platinum, gold, silver and palladium within LDA using energy cut-off of 560eV. This was done in order to investigate their effect on the geometric parameters of pure anatase. Figures 3.26 to 3.29 shows the conventional unit structures of Pt, Au, Ag, and Pd interstitially doped anatase. Table 3.8 presents their structural parameters, where all *a* lattice parameters increases with doping (as expected). The lattice *c* parameters of doped anatase all decrease to varying extents compared with the pure anatase. The overall effect is an increase of volume with Pd and Ag inducing the least and most changes respectively.

**Table 3.8: Geometric parameters of undoped and doped $TiO_2$ anatase.**

| | $TiO_2$ | $Ti_2PtO_4$ | $Ti_2AuO_4$ | $Ti_2AgO_4$ | $Ti_2PdO_4$ |
|---|---|---|---|---|---|
| a (Å) | 3.803 | 4.022 | 4.092 | 4.100 | 4.034 |
| c (Å) | 9.808 | 9.743 | 9.438 | 9.659 | 9.651 |
| Volume ($Å^3$) | 141.8 | 157.6 | 158.0 | 162.4 | 157.1 |

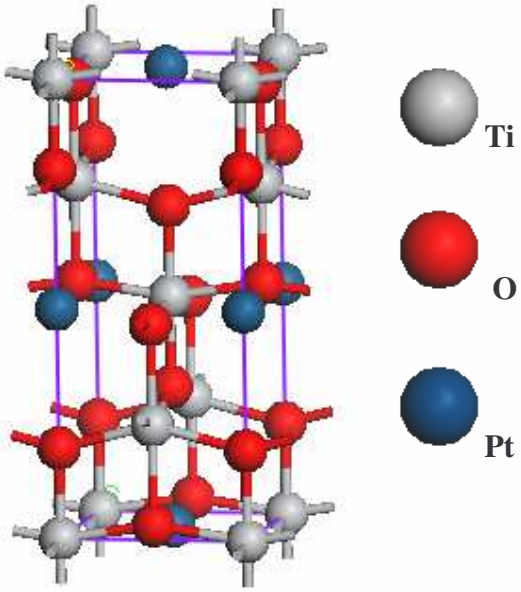


**Figure 3.26: Structure of anatase doped interstitially with platinum (Pt).**

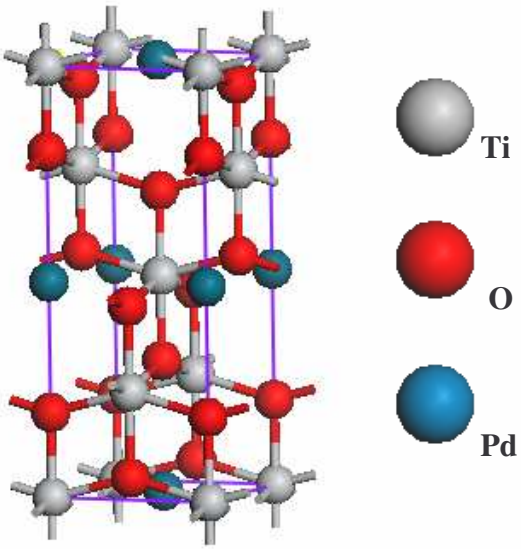


**Figure 3.27: Structure of anatase doped interstitially with palladium (Pd).**

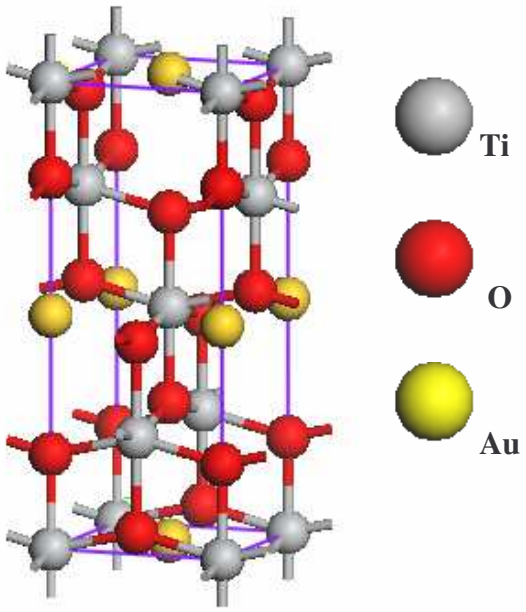


**Figure 3.28: Structure of anatase doped interstitially with gold (Au).**

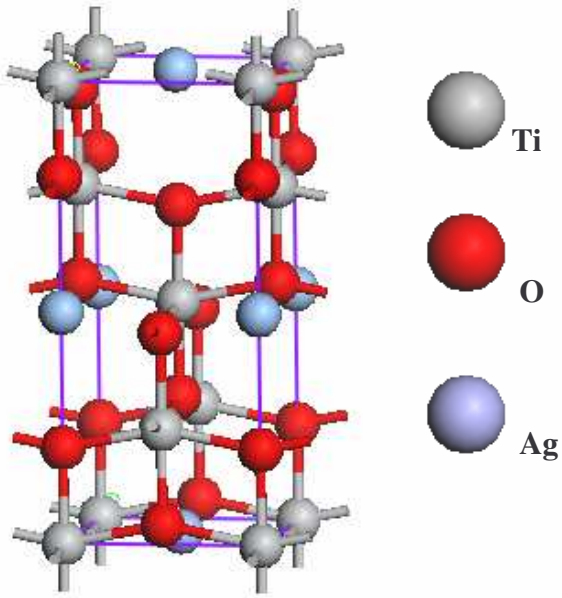


**Figure 3.29: Structure of anatase doped interstitially with silver (Ag).**

Solar irradiation can be used if a photocatalyst has a high reactivity under visible light. From section 1.3.2 we noted that doping enhances optical properties of anatase, hence it is expected that precious metal doped anatase will have increased absorption (A) and reflectivity (R) in the visible region between 400nm and 600nm. Firstly we relaxed the primitive structure of $TiO_2$ by performing geometry optimization calculations using energy cut-off of 700eV. Table 3.9 presents our calculated structural parameters at cut-off of 560eV and 700eV together with experimental results (Burdett et al 1987). There is no much effect with the increase of energy cut-off on the structural parameters.

**Table 3.9: Optimized structural parameters of anatase at cut-off of 560eV and 700eV compared to experiment (Burdett et al 1987).**

| | This work | | Exp. |
|---|---|---|---|
| | 560eV | 700eV | |
| a (Å) | 3.803 | 3.802 | 3.782 |
| c (Å) | 9.808 | 9.808 | 9.502 |
| c/a | 2.579 | 2.580 | 2.512 |
| $d_{eq}$ | 1.955 | 1.955 | 1.932 |
| $d_{ap}$ | 1.996 | 1.997 | 1.979 |
| Volume ($Å^3$) | 141.8 | 141.8 | 136.2 |

In section 3.2.3 it was shown that calculated absorption (figure 3.10) of $TiO_2$ agrees well with the experimental results. We now compare doped spectra with our calculated spectrum of pure anatase. Figure 3.30 presents the absorption spectra of anatase and transition doped anatase with energy cut-off of 700eV. Now pure anatase and transition doped anatase have the same absorption of $170x10^3$ at wavelength of 200nm. Between wavelength of 200nm and 300nm all transition doped anatase have almost the same behaviour, they decrease with the same trend. Some overlap while pure anatase is having higher absorption. All transition metals doped anatase increases

absorption in the visible region. Pt increases absorption more than other elements and the trend is as follows: $A_{Pt}>A_{Pd}>A_{Au}>A_{Ag}>A_{pure}$. Pt and Pd are almost close to each other especially after visible region, while Au and Ag are close to each other after visible region.

Figure 3.31 presents the reflectivity spectra of anatase and transition doped anatase with energy cut-off of 700eV. At wavelength of 200nm all spectra have reflectance of approximately 0.33, and between 200nm and 300nm they have almost constant reflectance, with that of pure anatase higher. In the visible region Pt and Pd increase the reflectivity while Au has almost the same reflectance as the pure anatase. Above visible region Pt and Pd have almost the same reflectivity, while those of Au and Ag are reduced but similar. The trend is as follows: $R_{Pt}>R_{Pd}>R_{Au}>R_{Ag}>R_{pure.}$

From absorption and reflectivity plots we note that the optical properties of the precious metal doped anatase are in most cases enhanced in the visible region. This is in good agreement with the experimental results (Fuerte et al 2001). In our study Pt enhances the optical properties the most. Figure 3.30 and 3.31 clearly suggest that optical properties in the precious metals doped anatase are enhanced in the visible region, in agreement with the calculations and the experiments discussed in section 1.3.2. Our results are in good agreement with the plots of reflectance against wavelength (nm) (Fuerte et al 2001); however, Fuerte et al (2001) doped $TiO_2$ with different transition metals as compared to our transition metals.

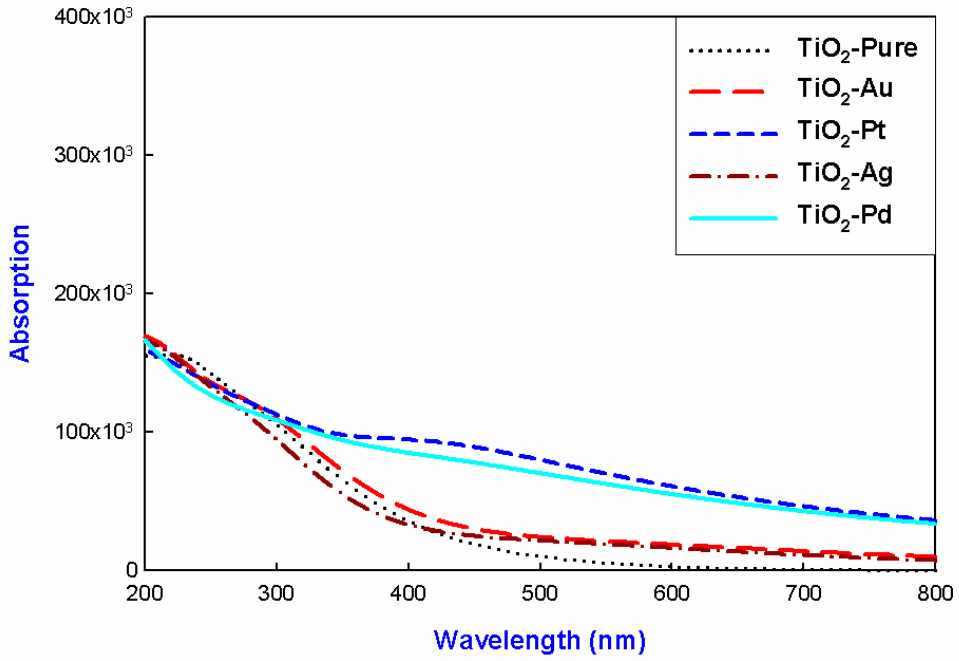


**Figure 3.30: Calculated absorption spectra of anatase and Pt-Au-Ag-Pd doped anatase, for 700eV energy cut-off.**

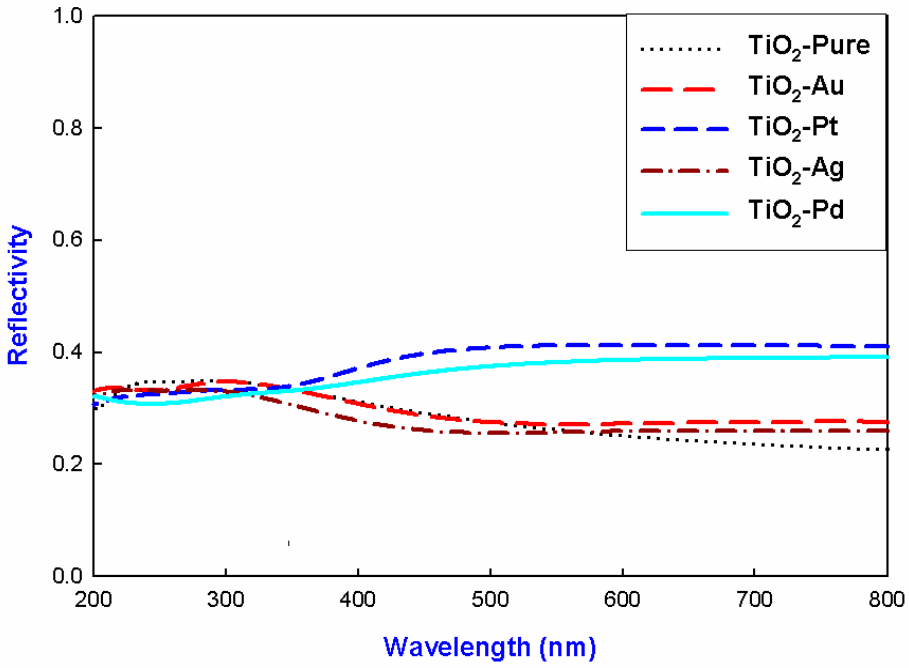


**Figure 3.31: Calculated reflectivity spectra of anatase and Pt-Au-Ag-Pd doped anatase, for 700eV energy cut-off.**

Since Pt enhances R and A better than other precious metal elements, it was chosen for doping anatase interstitially and substitutionally. We doped anatase interstitially with two atoms of Pt and we have substituted Ti atom(s) in different ways and with different concentration to study their effect on optical properties (reflectivity and absorption). We have substituted one atom of Ti with Pt at the corner, centre and side. We have further substituted two atoms of Ti with Pt on the same structure of anatase, one at the centre and the other at a corner. The corresponding structures are shown in figures 3.32- 3.35. Figure 3.36 presents the absorption spectra of pure anatase and doped anatase with Pt located at different sites. At the wavelength of 200nm all the spectra have absorption of $170x10^3$. Between the wavelength of 200nm and 300nm absorption of all spectra decrease with wavelength and in particular that of pure $TiO_2$ is the highest. Beyond 300nm all types of doping enhance the magnitudes of absorption spectra above that of pure anatase. Substituting Ti with more concentration of Pt increases absorption spectra of anatase more than other kind of doping in the visible region. Absorption spectra corresponding to substitution of Ti by Pt on the corner, side and centre are similar and they overlap each other. Interstitial doping with Pt increases absorption spectra of anatase more than substituting with one atom. Figure 3.37 presents the reflectivity spectra of pure anatase and Pt doped anatase in different kinds of doping. At the wavelength of 200nm all spectra have reflectance of 0.33. Between wavelength of 200nm and 400nm pure anatase has high reflectivity than all doped spectra. In the visible region, substituting anatase with two Pt atoms and interstitial doping increases reflectivity of anatase above 400 nm respectively. Substitution of one Ti by Pt atom at various sites yields similar reflectivity spectra, but the related magnitudes exceed that of pure anatase above 570nm.

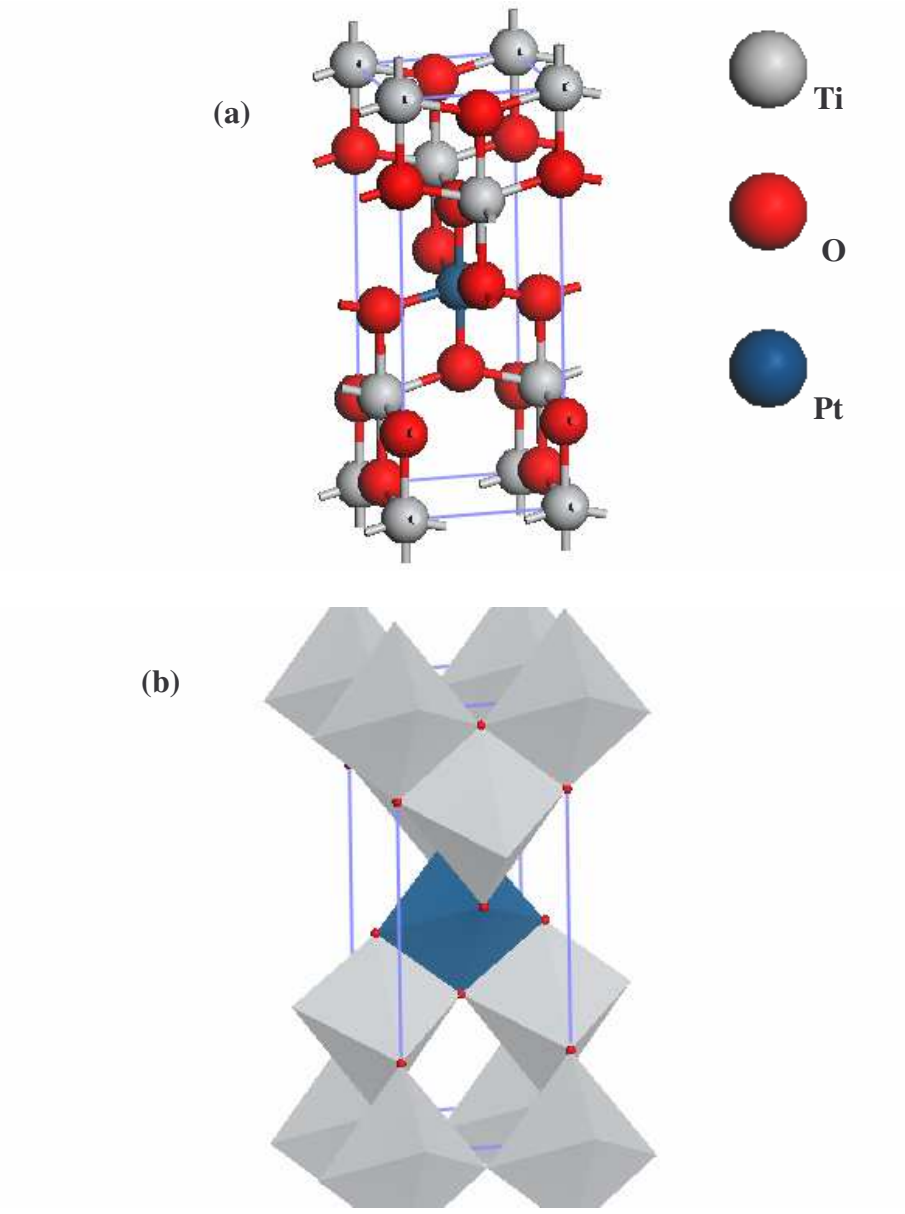


**Figure 3.32: Structure of anatase doped subsitutionally with Pt at the centre (a) conventional (b) polyhedron.**

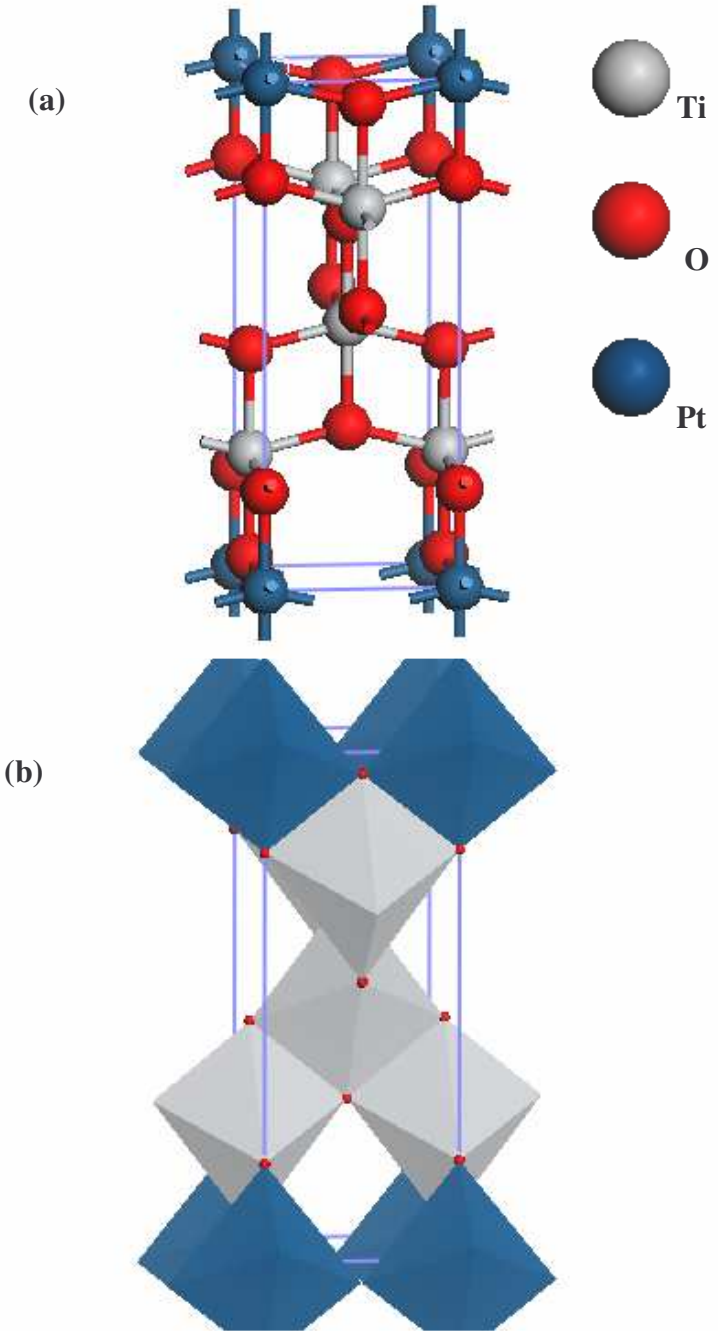


**Figure 3.33: Structure of anatase doped subsitutionally with Pt at the corner (a) conventional (b) polyhedron.**

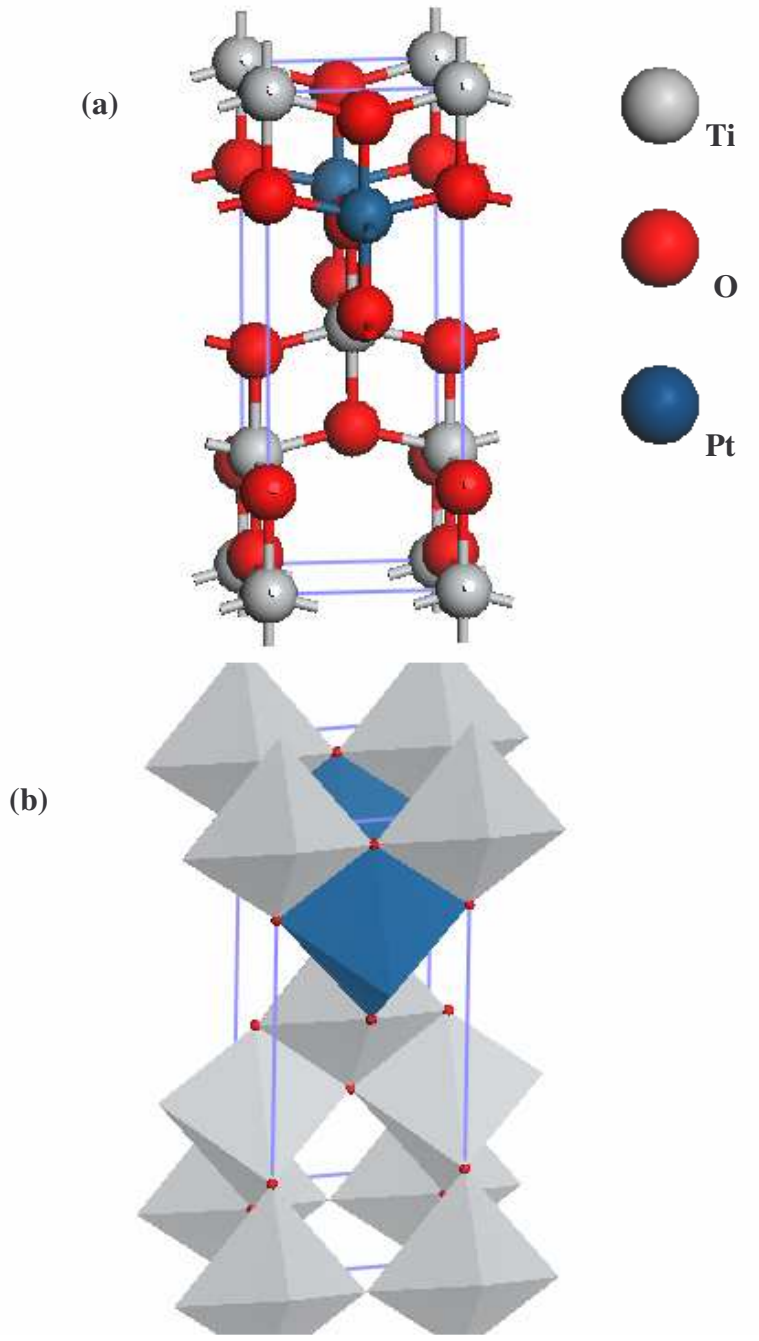


**Figure 3.34: Structure of anatase doped subsitutionally with Pt at the sides (a) conventional (b) polyhedron.**

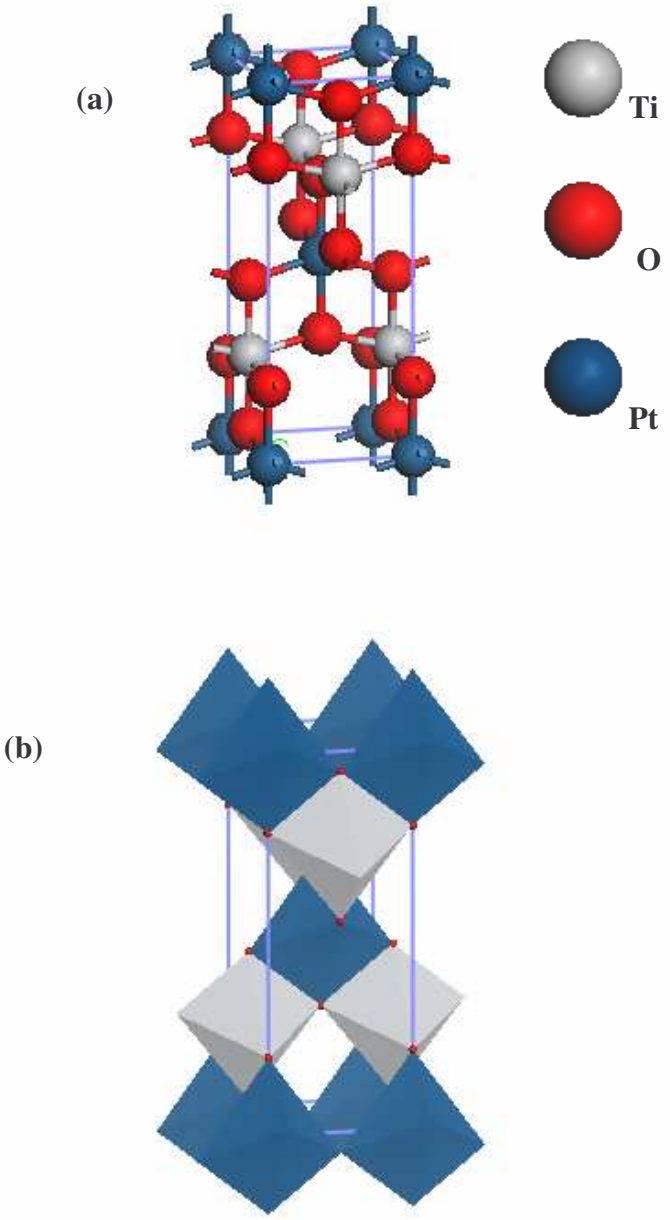


**Figure 3.35: Structure of anatase doped subsitutionally with Pt at the centre and corner (a) conventional (b) polyhedron.**

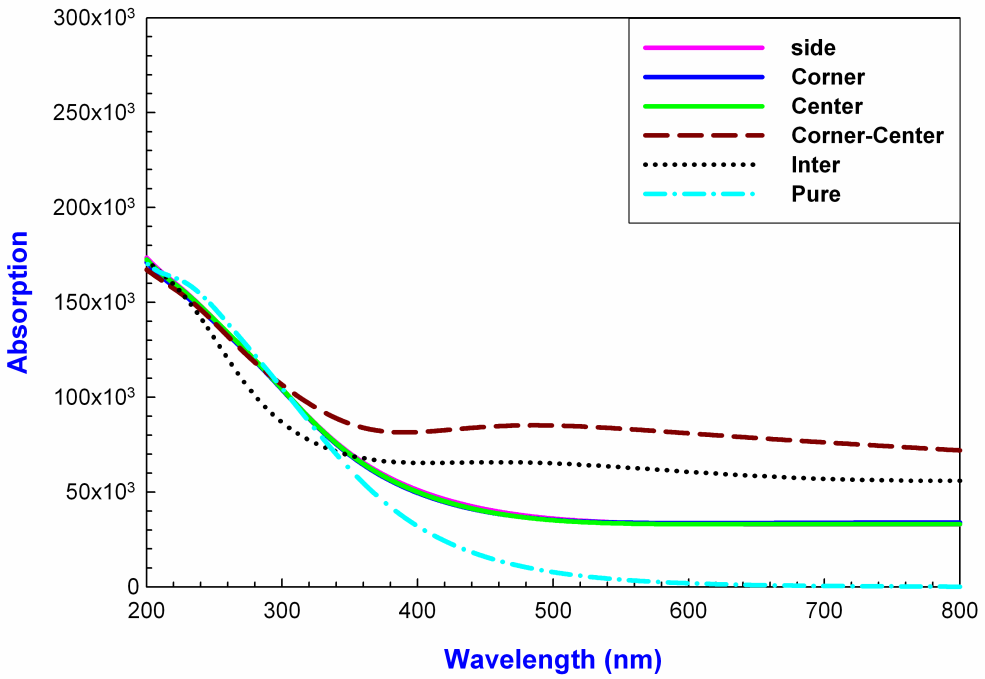


**Figure 3.36: Calculated absorption spectra of anatase with different kinds of doping with Pt.**

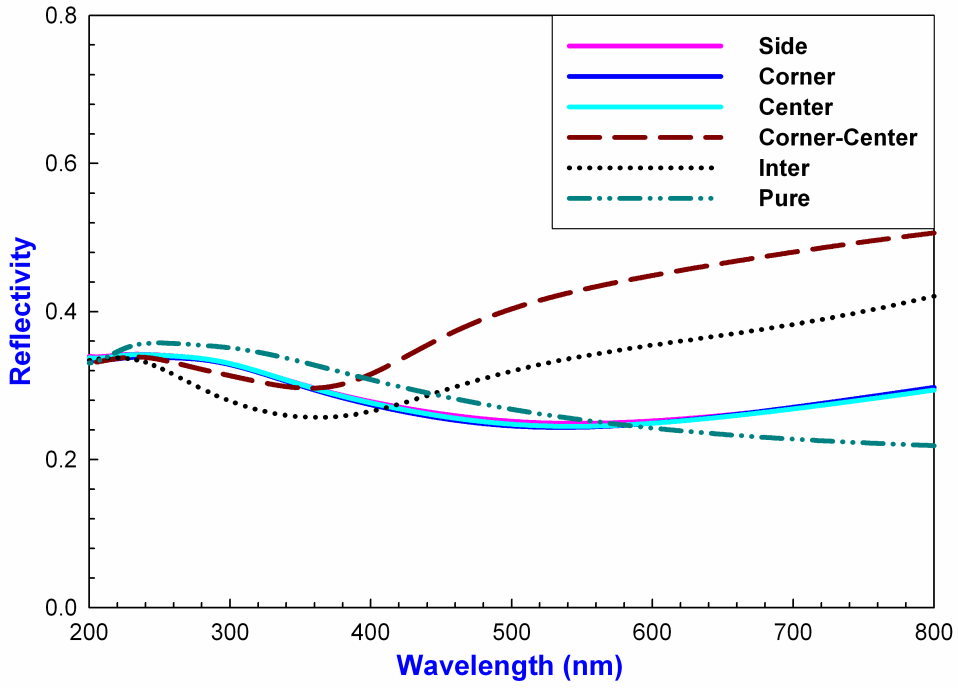


**Figure 3.37: Calculated reflectivity spectra of anatase with different kinds of doping with Pt.**

### 3.4.2 Density of states

This section presents total and partial densities of states of precious metals doped anatase interstitially and substituting with two atoms. Figure 3.38 shows the total and partial DOS for Pt doped anatase at interstitial position. The total DOS consists of two peaks at about -20eV and -18eV and a broader peak varying from -10eV to -2eV in the valence band. The peaks located at about -20eV and -18eV are predominantly from $O_{2s}$, the broader peak indicates a strong hybridization between $O_{2p}$ and $Pt_{5d}$, while the $Ti_{3d}$ shows less contribution as evident from the partial DOS plots. There is a single peak observed at about -2eV which is a contribution of $Pt_{5d}$. More importantly, the Fermi level lies on the left shoulder of the peak (which is a contribution of $Ti_{3d}$) at $E_f$ =0 and there is no band gap observed but only a pseudogap. We also note that the Fermi level is being shifted away from the pseudogap. This shows that interstitially doping anatase with Pt renders the system metallic, since in section 3.2.1 the undoped anatase is observed as an insulator. Since the Fermi level falls into the pseudogap it shows a stable structure. The conduction band consists of two broad peaks at about 2eV and 8eV. The conduction band peak located at about 2eV is mainly contribution of $Ti_{3d}$ and $Pt_{5d}$, while the peak at 8eV consists of $Pt_{5p}$ and a lower $Ti_{3p}$.

Figure 3.39 shows the total and partial DOS for Au doped anatase at the interstitial position. They show similar trends as compared to figure 3.38, except that there is no single peak observed -2eV. The broader peak varying from -10eV to -2eV is the hybridization between $O_{2p}$ and $Au_{5d}$ with less contribution of $Ti_{3d}$. The pseudogap observed near $E_f$ is narrow and deeper as compared to figure 3.38, due to the contribution of $Au_{5d}$. This indicates that interstitial doping anatase with Au also renders the system as metallic.

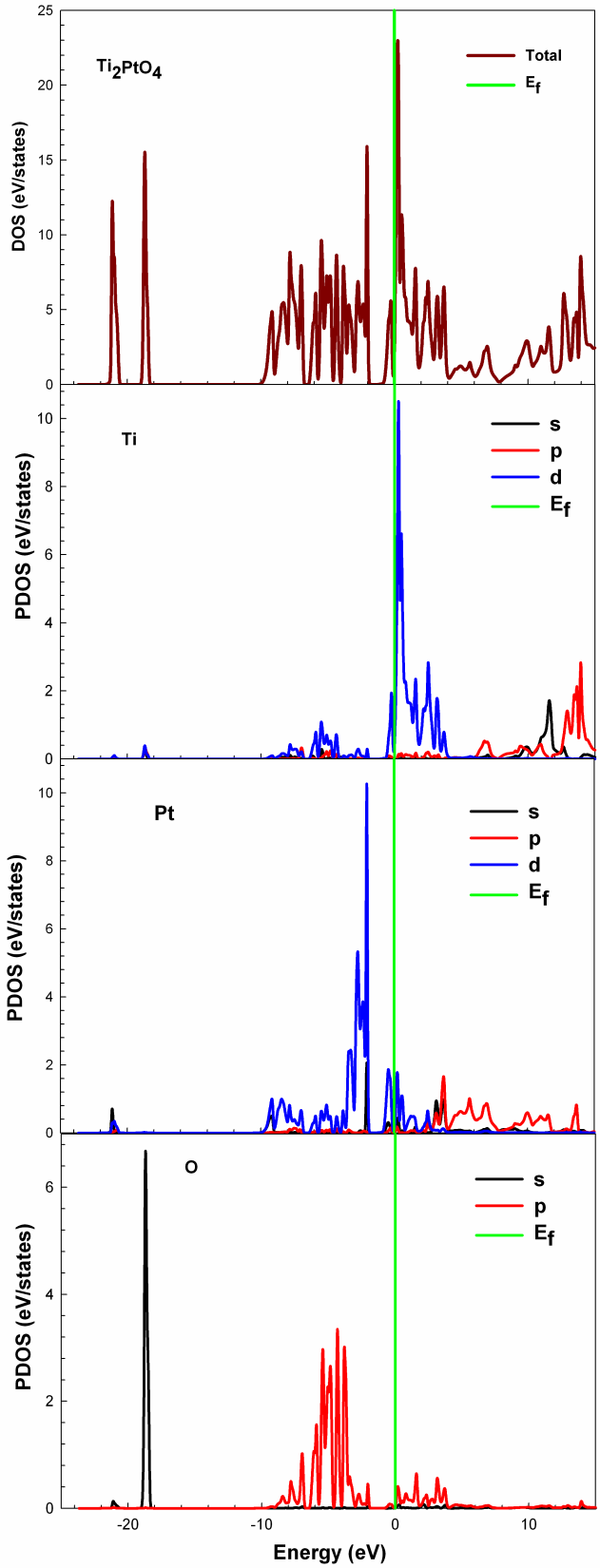


**Figure 3.38: Total and partial DOS of anatase doped interstitially with Pt. The Fermi energy is taken as the energy zero ($E-E_f=0$).**

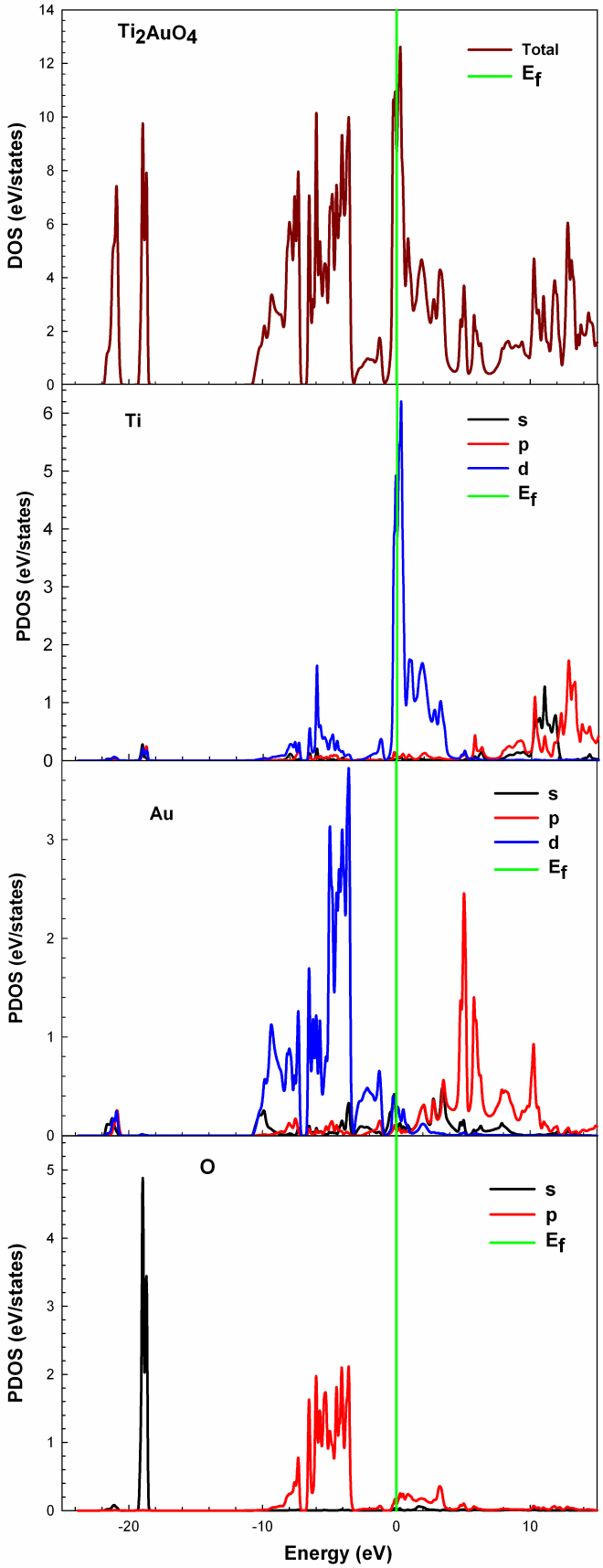


**Figure 3.39: Total and partial DOS of anatase doped interstitially with Au. The Fermi energy is taken as the energy zero ($E-E_f=0$).**

Figure 3.40 shows total and partial DOS of Ag doped anatase at interstitial position. Again DOS plots show similar trends as in the previous figures, and no single peak is observed at around -2eV. Instead a small peak is observed which contributed to the formation of the pseudogap near $E_f$. The broader peak at around -2eV is the contribution of $Ag_{4d}$ and $O_{2p}$ with less hybridization. The pseudogap is broader as compared to that observed in figure 3.39. Again we observe that Fermi level lies on the left shoulder of the $Ti_{3d}$ peak suggestion of instability. Ag doped anatase renders the system as metallic.

Figure 3.41 present the total and partial DOS of Pd doped anatase at interstitial position. We note that the Fermi level lies on the right shoulder of the small peak, in contrast to the cases of Pt, Au and Ag. More interestingly the $E_f$ slightly falls in the pseudogap which is narrowed. Since the Fermi level falls into the pseudogap it shows a stable structure. Similarly to the case of Pt, Au and Ag, the Pd doped anatase renders a system as a metallic.

Figure 3.42 shows the total and partial DOS of Pt doped anatase substitutionally. Here we have substituted two Ti atoms by introducing the equivalent of Pt atoms (the structure is shown in figure 3.35.) and the structure has the composition $TiPtO_4$. In the case of substitutional doping the double peak at around -20eV has not been resolved, contrary to the interstitial doping (figure 3.38), where two peaks were observed. We further observe a broader peak ranging from -10eV to 0eV which is the contribution of $Pt_{5d}$ and $O_{2p}$. More importantly, $E_f$ fall directly into the pseudogap which is narrowed as compared to figure 3.38 suggestion of stability. The pseudogap is characterized by a small peak in the conduction band and large peak in the valence band, emanating from a hybridization of $Pt_{5d}$ and $O_{2p}$. In addition the $E_f$ lies further away from the $Ti_{3d}$ peak as compared to that in figure 3.40 which is closer. The

system has a metallic behaviour. In the conduction band a broader peak is observed, which is a contribution of $Ti_{3d}$, $Pt_{5p}$ and less contribution of $O_{2p}$.

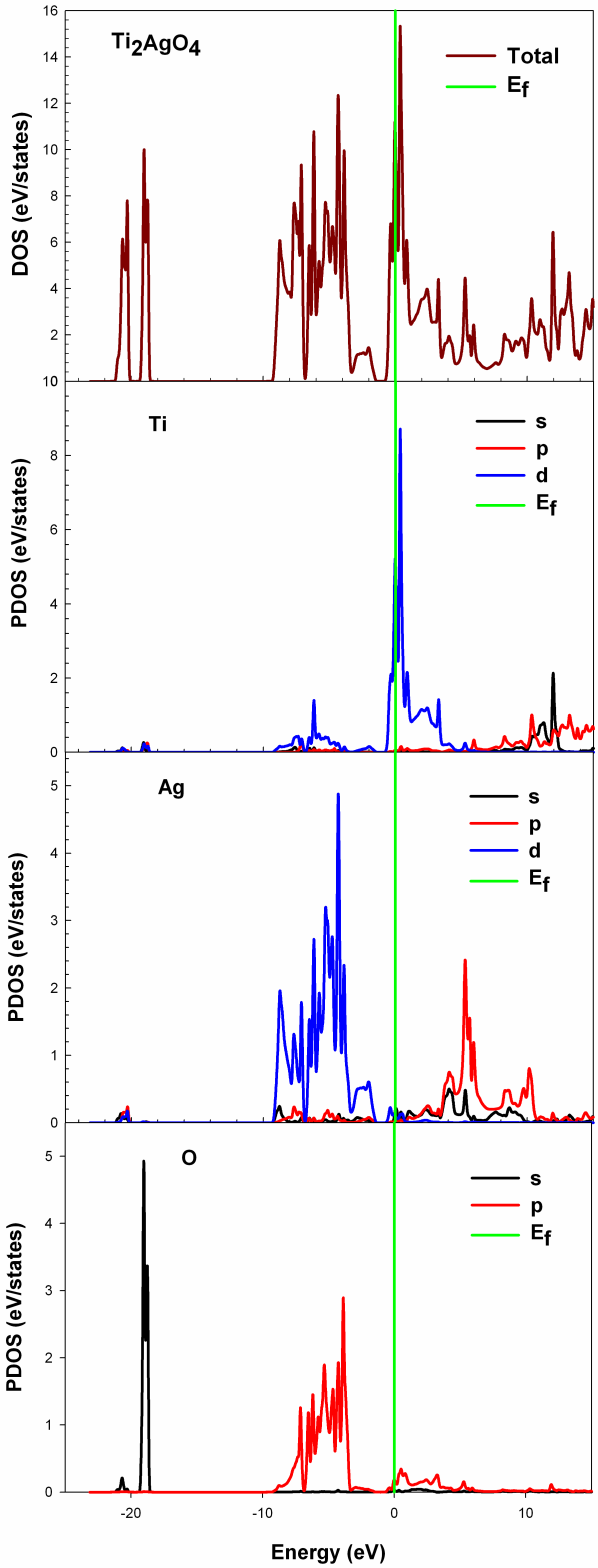


**Figure 3.40: Total and partial DOS of anatase doped interstitially with Ag. The Fermi energy is taken as the energy zero ($E-E_f=0$).**

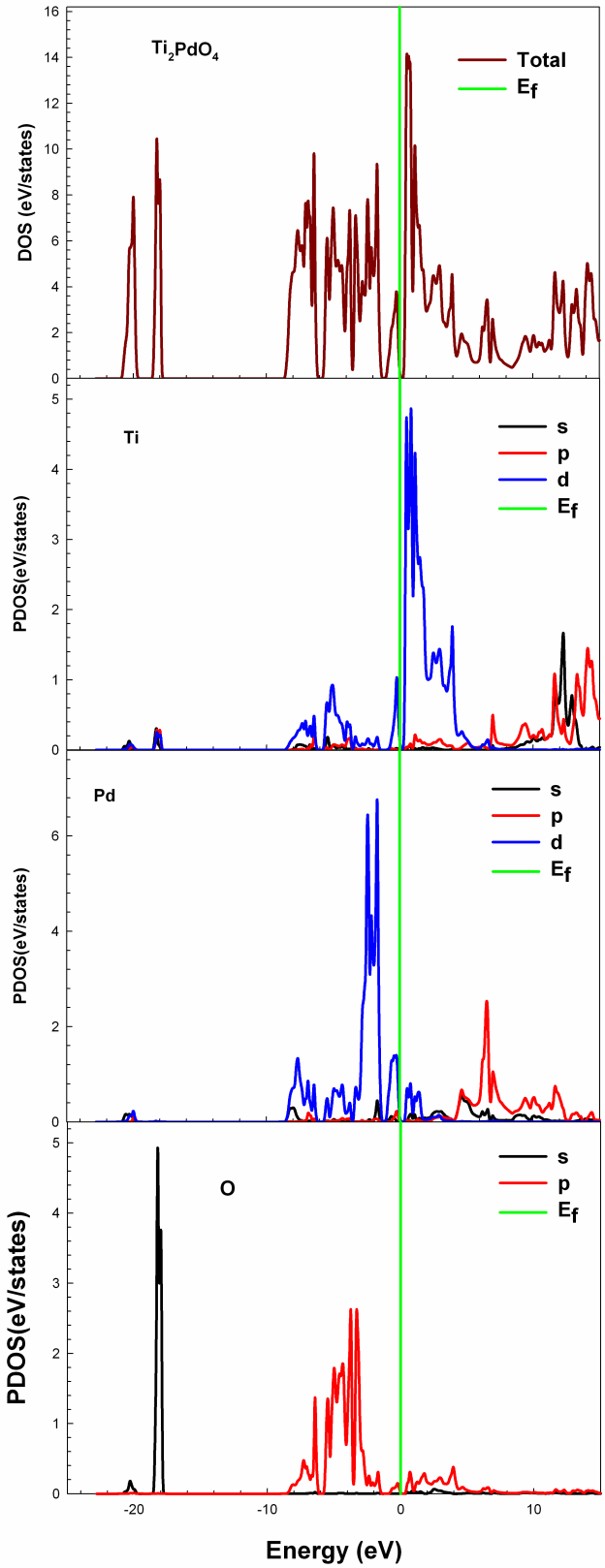


**Figure 3.41: Total and partial DOS of anatase doped interstitially with Pd. The Fermi energy is taken as the energy zero ($E-E_f=0$).**

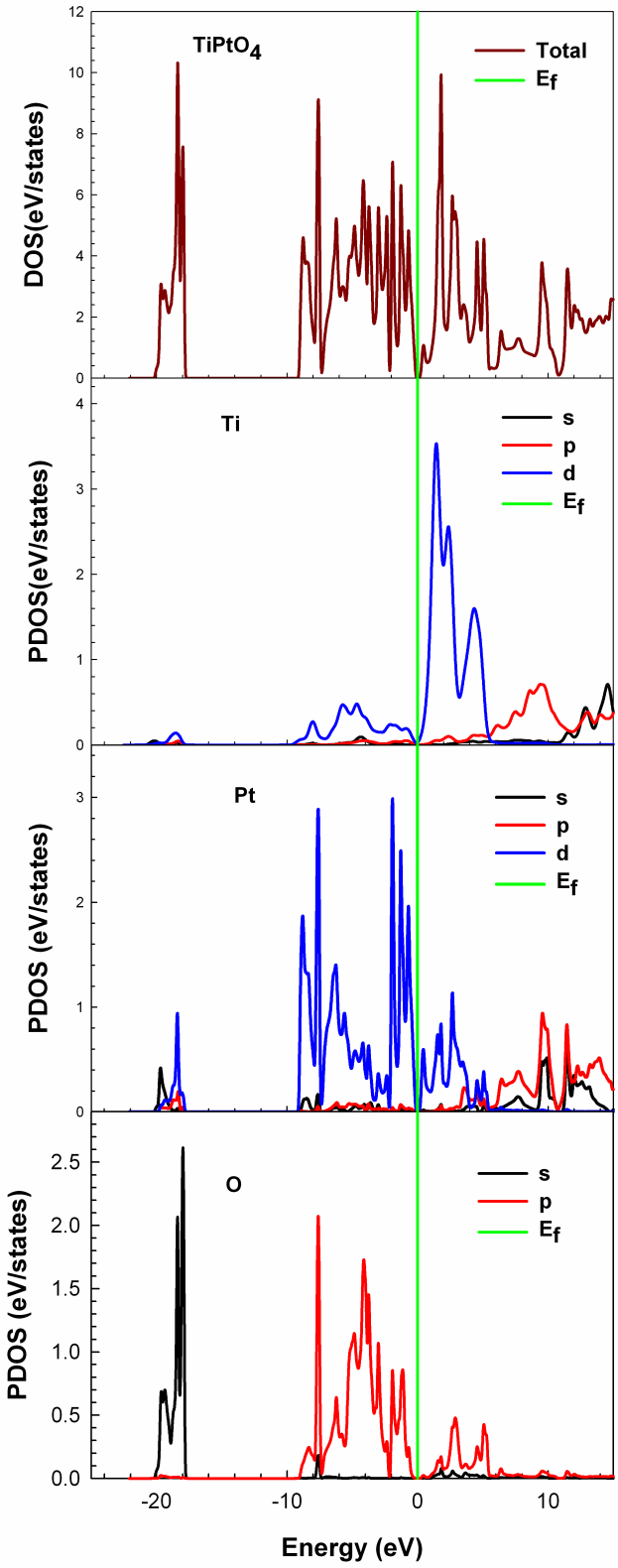


**Figure 3.42: Total and partial DOS of anatase doped substitution with two atoms of Pt. The Fermi energy is taken as the energy zero ($E-E_f=0$).**

## 3.5 Charge density difference

Figure 3.43 presents charge density difference for interstitial doped anatase ($Ti_4Pt_2O_8$), (a) showing the Ti-O and (b) the Pt-O bonding, respectively. Charge density difference around Pt and O atoms has a blue colour which indicates a charge loss, while Ti atoms are surrounded by a red colour which shows charge gain. This observation is supported by mulliken population analysis in table 3.10 (column 2). We note that Ti (2) is more reactive with O (2) and O (4) than Ti (1) as shown by positive values of 0.81|e| and 0.53|e|, respectively. There is an anti-bonding reaction between O atoms, which is shown by a negative value of -0.06|e| and -0.13|e|. Furthermore, we note an anti-bonding behaviour between Ti (1) and Pt (1) atoms with the value of -0.71|e|.

**Table3.10: Mulliken Population analysis of M doped $TiO_2$ interstitially (M = Pt, Au, Ag, Pd). The dashed lines indicate that no population was attained.**

| Bond | $Ti_4Pt_2O_8$ | $Ti_4Au_2O_8$ | $Ti_4Ag_2O_8$ | $Ti_4Pd_2O_8$ |
|---|---|---|---|---|
| Ti1-O1 | 0.50 | 0.52 | 0.50 | 0.64 |
| Ti1-O2 | 0.53 | 0.50 | 0.45 | 0.53 |
| Ti1-O3 | 0.50 | 0.52 | 0.50 | 0.64 |
| Ti1-O4 | 0.53 | 0.50 | 0.45 | 0.54 |
| Ti2-O2 | 0.81 | 0.81 | 0.81 | 0.89 |
| Ti2-O3 | 0.20 | 0.20 | 0.24 | 0.30 |
| Ti2-O4 | 0.81 | 0.81 | 0.81 | 0.89 |
| Ti1-M1 | -0.71 | -0.90 | -0.60 | -1.23 |
| O1-M1 | 0.15 | 0.08 | 0.28 | 0.02 |
| O2-M1 | ---- | -0.16 | -0.08 | ---- |
| O3-M1 | 0.15 | 0.08 | 0.28 | 0.02 |
| O4 -M1 | ---- | -0.16 | -0.08 | ---- |
| O1-O3 | -0.06 | -0.09 | ---- | -0.06 |
| O2-O4 | ---- | ----- | ---- | -0.06 |
| O3-O4 | -0.13 | -0.11 | -0.10 | -0.14 |

Figure 3.44 shows charge density difference for interstitial doped anatase ($Ti_4Au_2O_8$), (a) showing the Ti-O and (b) the Au-O bonding, respectively. The bonding between Ti-O is similar as above, however we observe less bonding between Au and O as shown by the blue colour, in figure 3.44 (b). From table 3.10 (column3) we note that the overlap population analysis shows anti-bonding between Au and O with the value of -0.16|e|.

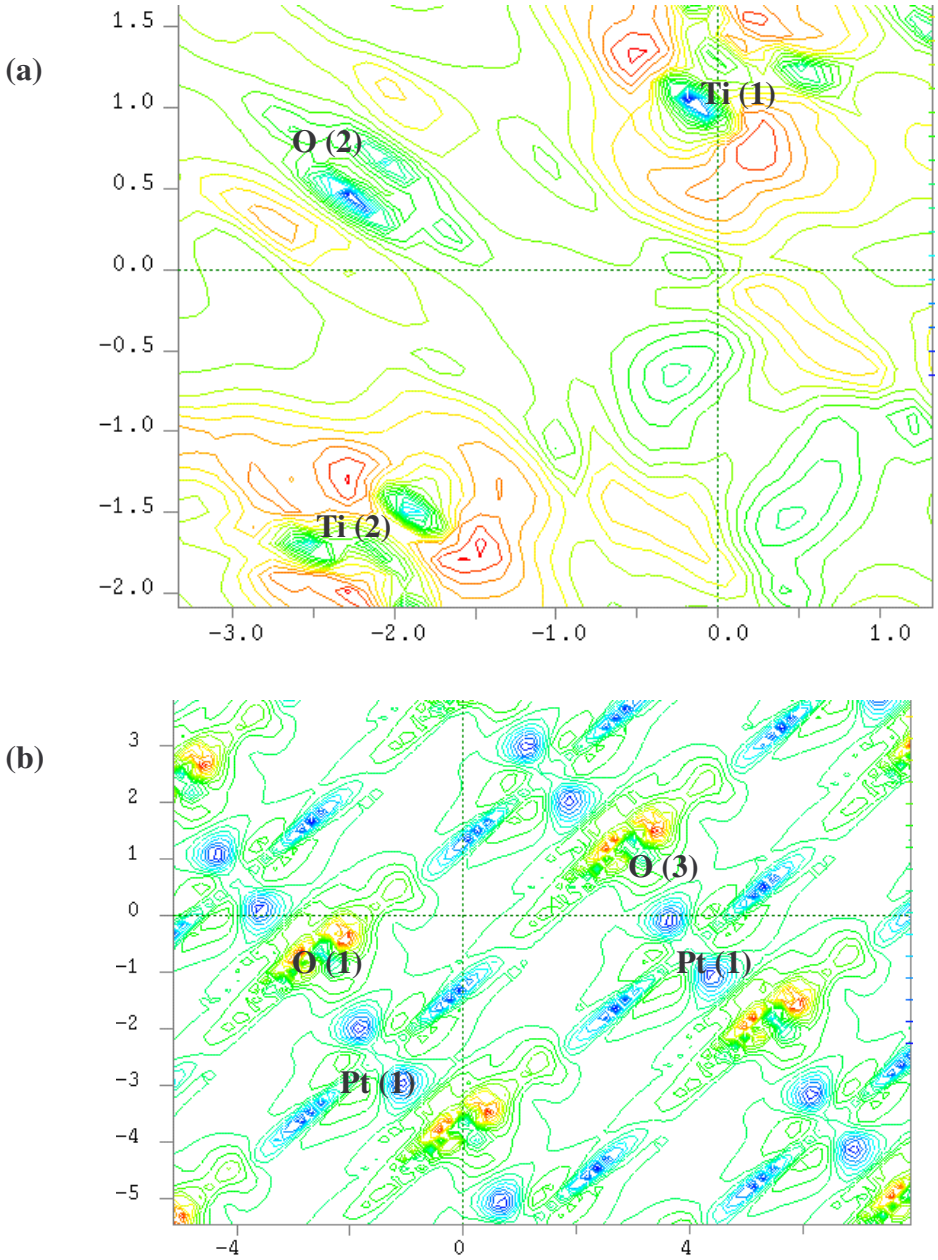


**Figure 3.43: The charge density difference plot of $Ti_4Pt_2O_8$ showing (a) Ti-O and (b) Pt-O bonding.**

It is also evident that O atoms bonds strongly with Ti than Au, since Ti-O is more positive than Au-O bond.

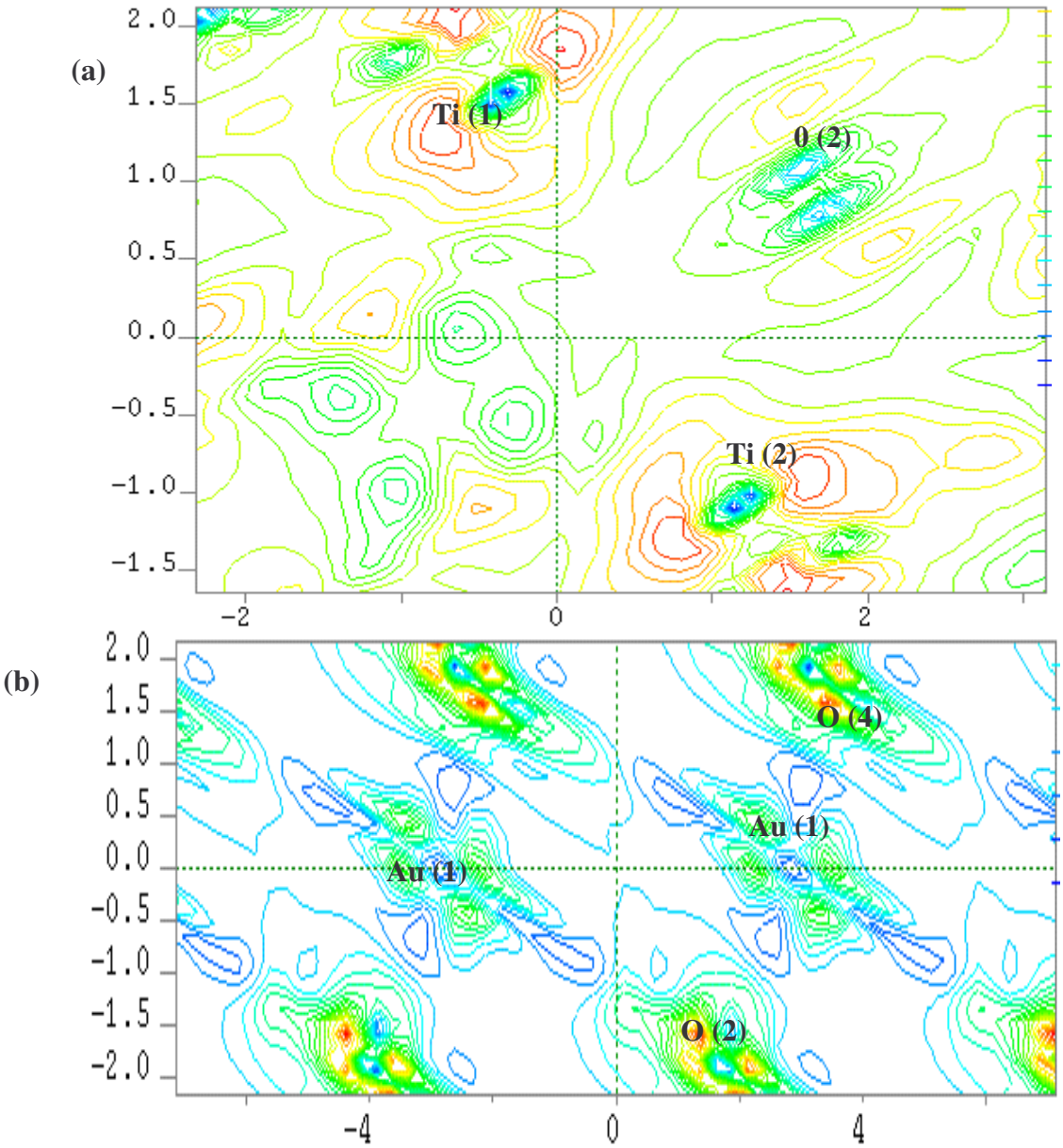


**Figure 3.44: The charge density difference plot of $Ti_4Au_2O_8$ showing (a) Ti-O and (b) Au-O bonding.**

Figure 3.45 presents charge density difference for interstitial doped anatase ($Ti_4Ag_2O_8$), (a) showing the Ti-O and (b) the Ag-O bonding, respectively. We note some charge loss around the Ti atoms as shown by blue colour (figure 3.45a), whereas Ag show charge gain (figure 3.45b). This is supported by overlap population analysis

in table 3.10 (column 4), which reveals the strong bonding behaviour of Ti(1)-O(1) and O(1)-Ag(1) with the values of 0.50|e| and 0.28|e|, respectively. This suggests that the O atoms react more positively with Ti than Ag metals. We also note an anti-bonding between Ti(1), O(2) with Ag(1) indicated by -0.60|e| and -0.08|e|, respectively.

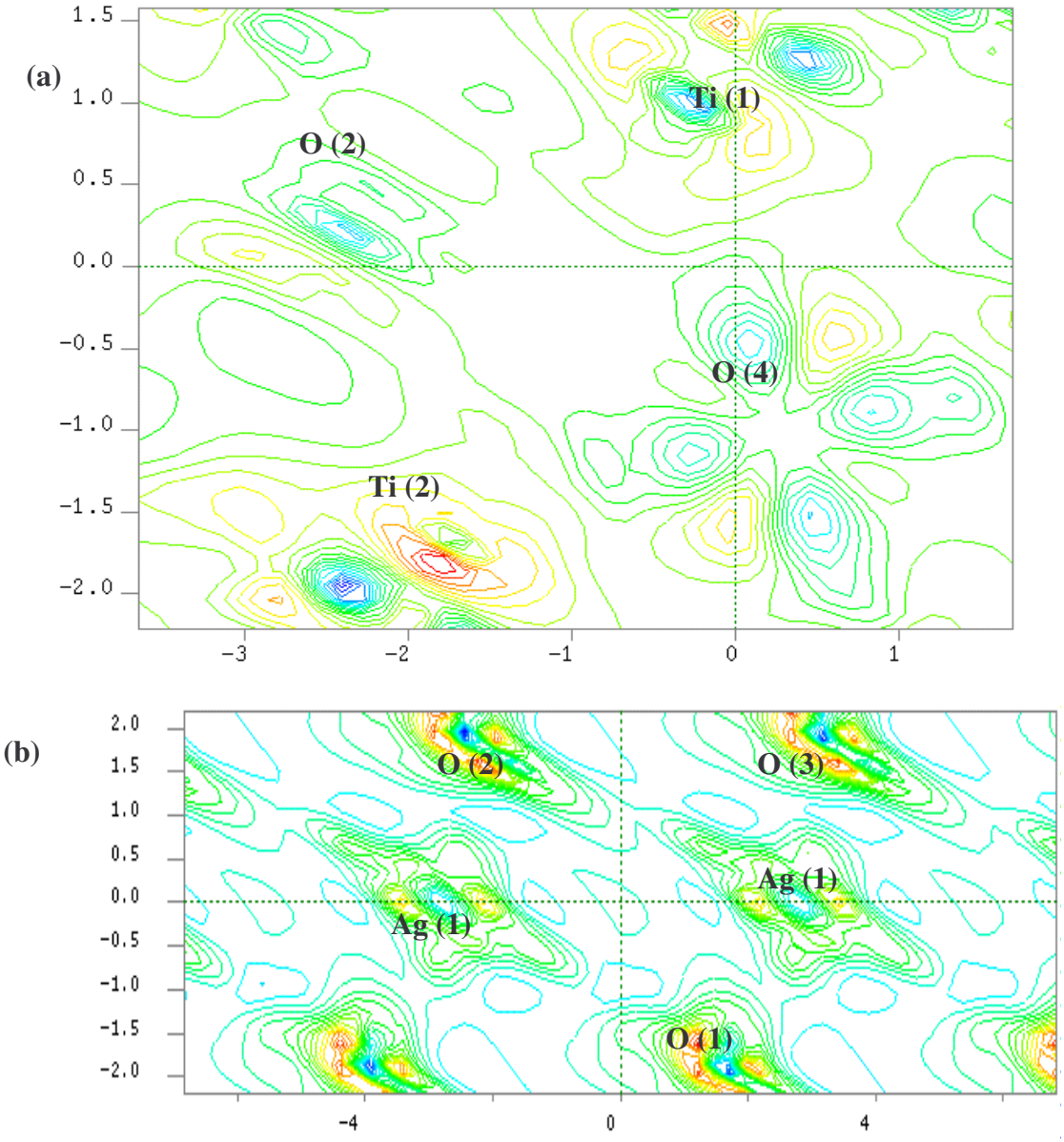


**Figure 3.45: The charge density difference plot of $Ti_4Ag_2O_8$ showing (a) Ti-O and Ag-O bonding.**

Figure 3.46 presents charge density difference for interstitial doped anatase ($Ti_4Pd_2O_8$), (a) showing the Ti-O and (b) the Pd-O bonding, respectively. In figure

3.46 (a) Ti shows a blue colour which indicate charge loss and O(2) is more red than O(1), indicating that O(1) has less charge than O(2). Figure 3.46 (b) shows that Pd is less reactive towards O because of the blue colour around Pd atoms. This agrees well with the overlap population analysis in table 3.10 (column5) where the value of Pd (1)-O (1) bond is 0.02|e|, which is less compared to the other metals discussed above. The atoms react more strongly with Ti than Pd with the value of 0.50|e|. There is an anti-bonding of Ti(1)-Pd(1) with the value of -1.23|e| and O-O with the value of -0.06|e| and -0.14|e|.

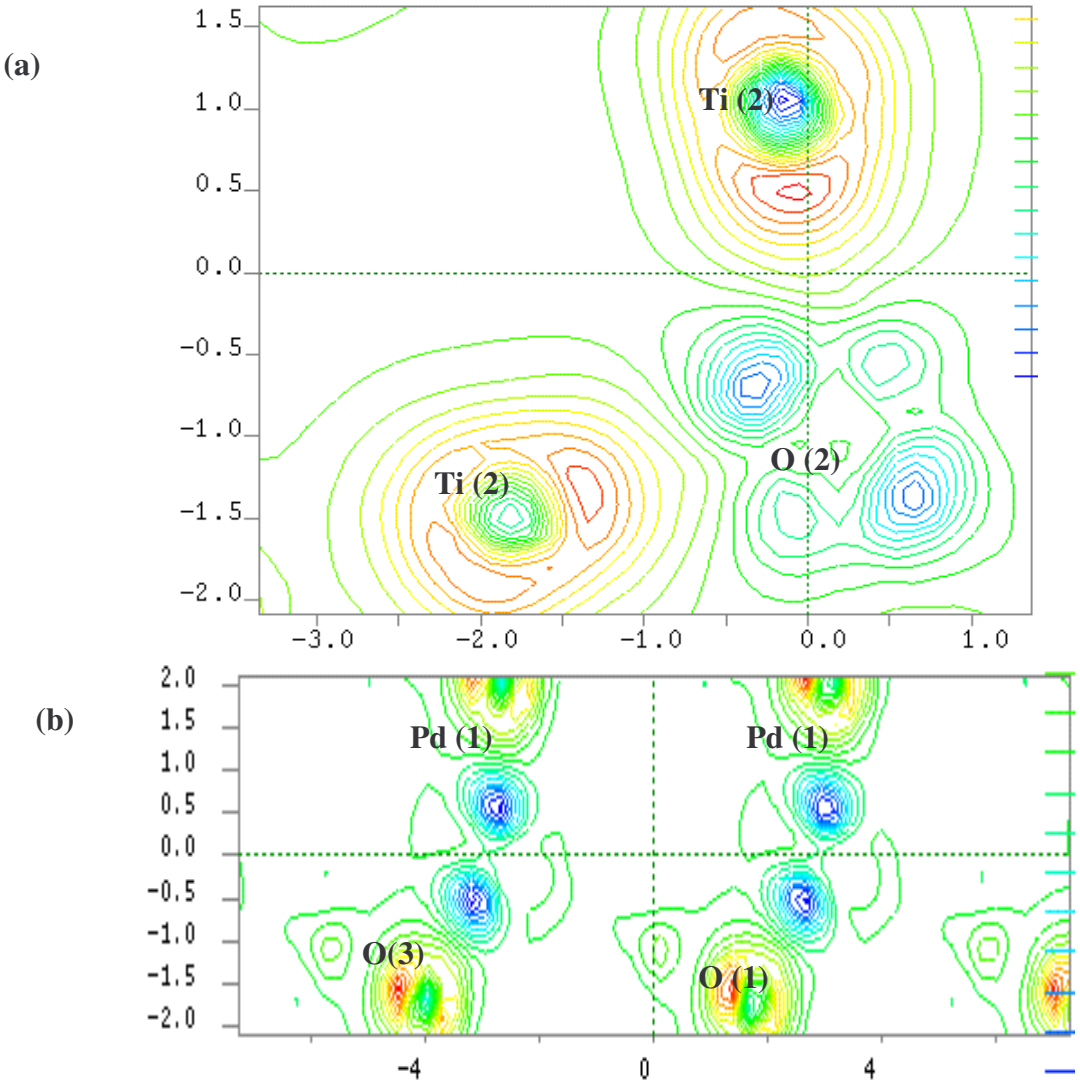


**Figure 3.46: The charge density difference plot of $Ti_4Pd_2O_8$ showing (a) Ti-O and Pd-O bonding.**

## 3.6 Heats of formation

In this section we present heats of formation ($\Delta H_f$) of pure anatase and precious metal doped anatase. Heats of formation determine the stability of our systems. The heats of formation have been calculated using CASTEP code. The heat of formation is determined by subtracting the total energies of the elemental systems from that of the compound. Subtracting the total energies we use the relation

$$\Delta H_f = \frac{1}{N}\left[E_{Total}(structure) - E_{Total}(1^{st}\ atom) - E_{Total}(2^{nd}\ atom)\right]$$

were N is the total number of atoms, $E_{Total}$ (structure) is the total energy of the system and the last two terms are total energy of individual atoms one and two. In order to calculate the heats of formation of $TiO_2$ the above equation takes the form

$$\Delta H_f(TiO_2) = \frac{1}{3}\left[E(TiO_2) - E(Ti) - 2E(O)\right]$$

Table 3.11 presents calculated heats of formation of undoped $TiO_2$, transition doped $TiO_2$ and the experimental heat of formation of $TiO_2$ from http://roger.ecn.purdue.edu/~propulsi/propulsion/comb/propellants.html. Heats of formation from this website are in ca/g so we have converted them to eV.

**Table 3.11: Heats of formation of $TiO_2$ and doped $TiO_2$.**

| | Exp (eV) | CASTEP (eV) |
|---|---|---|
| $TiO_2$ | -8.86 | -7.75 |
| $Ti_4Pt_20_8$ | -------- | -5.36 |
| $Ti_4Au_2O_8$ | ---------- | -4.90 |
| $Ti_4Ag_2O_8$ | ---------- | -5.14 |
| $Ti_4Pd_2O_8$ | ---------- | -5.26 |
| $Ti_2Pt_2O_8$ | -------- | -5.11 |

Heat of formation of $TiO_2$ calculated from CASTEP is close to the experimental

value. Calculated heat of formation indicates the stability of $TiO_2$. We do not have the experimental heats of formation for transition metal doped anatase, but all calculated heats of formation indicate the stability of interstitial doped anatase. By comparing heats of formation substitution and interstitially doping we notice that interstitial doping shows more stability than substitution. All heats of formation are negative implying stable structures.

# Chapter 4
# Conclusion

### *Structure relaxation*

Optimized structure of anatase was obtained by energy minimization. The equilibrium lattice parameters are in good agreement with the experimental values. Their difference is very small within 5% and, also bond lengths are very much close to the experimental values. All calculated bond angles are smaller as compared to the original angles by a small amount. Optimized atomic positions of Ti and O atoms are similar to the original positions.

### *Electronic and optical properties of $TiO_2$*

Our calculated density of states (DOS) for pure anatase is in reasonable agreement with the experiment and our band gap is 2.0eV being 1.2eV smaller than the experimental gap value of 3.2eV. From DOS we observed that $TiO_2$ is an insulator. Our calculated optical properties of $TiO_2$ are in good agreement with the experimental results.

### *Equation of state and pressure dependence on parameters*

Our calculated parameters at zero pressure agree well with the experimental. Graphs of lattice parameters and the ratio against pressure, show that as the pressure increases our system become compressed. This compressibility of our system agrees well with the experimental results. Our bulk modulus was found to be 178.9GPa which agrees well with the experimental one which is 179GPa.

### *Transition metals doped $TiO_2$*

Transition metals (Pt, Au, Ag and Pd) doping enhances reflectivity and absorption of anatase in the visible region i.e. above 400nm. Hence Pt increases reflectivity and

absorption more than the other elements at energy cut-off of 700eV. The Fermi level of Pt doped $TiO_2$ and Pd doped $TiO_2$ falls into the pseudogap indicating the stability of structures. Fermi level of Au doped $TiO_2$ and Ag doped $TiO_2$ intercepts the total DOS curve at the top indicating the instability of the structure. From pDOS, d-orbital dominates more than other orbital and the total DOS shows that $TiO_2$ is a semiconductor. Total DOS for doped anatase shows that our system is a conductor.

### *Charge density difference*

The charge density difference of the interstitially doped anatase with Pt, Au, Ag and Pd, showed similar bonding behaviour and a distinction is drawn from the Mulliken population data (table 1.3). The $Ti_4Pd_2O_8$ shows that Ti-O is more reactive with the value of 0.64|e|, while the $Ti_4Pt_2O_8$ and $Ti_4Au_2O_8$ are almost similar. Furthermore, it has been noted that O reacts more with Ti than Pt atoms. Charge density difference for Pt-O shows low level of bonding between Pt and O atoms and an anti-bonding interaction between O atoms. The highest anti-bonding behaviour is noted for $Ti_4Au_2O_8$ with -0.90|e| and the lowest is observed for $Ti_4Pt_2O_8$ and $Ti_4Pd_2O_8$ compositions, with -0.06|e|.

### *Heats of formation*

Calculated heat of formation of $TiO_2$ agrees well with the experimental value. Transition metal doped anatase also indicates the stability of doped systems. Interstitial doping shows more stable than substitution.

# Bibliography


Arbiol J., Cerda J., Dezanneau G., Cirera A., Peiro F., Cornet A. and Morante, J. Appl. Phys. **92** 853 (2002).

Arlt T., Bermejo M., Blanco M. A., Gerward L., Jiang J. Z., Staun Olsen J. and Recio J. M., Phys. Rev. **61** 14 414 (2002)

Asahi R., Morikawa T., Ohwaki T., Aoki K. and Taya Y., Science, **293** 269, DOL:10.1126/science.1061051, (2001).

Barbe C.J., Arendse F.P., Comte, Jirousek M., Lenzmann F., Shklover V. and Gratzel M., J. Am. Cer. Soc., **80** 12 (1997).

Berger H., Tang H., and Tang F. Lévy, J. Cryst. Growth **130** 108 (1993).

Burdett J. K., Hughbanks T., Miller G. J., Richardson J. W.,Jr. and Smith J. V., J. Am. Chem. Soc. **109** 3639 (1987).

Chen Q. and Cao H. H., J. Mol. Struc. THEOCHEM **723** 135 (2005).

Fahmi A., Minot C., Silvi B., and Causa M., Phys. Rev. B **47** 11 717 (1993).

Fahmi A., Minot C., Silvi B., and Causa M., Phys. Rev. B **51** 13 023 (1995).

Fermi E., Z. Phys. **48** 73 (1928).

Freeman A. J. and Wimmer E. Annu. Rev. Mater. Sci. **25** 21 (1995).

Frondel C. The minerals of Franklin and Sterling Hill- a checklist. Wiley Interscience, New York, 94 (1972).

Fuerte A., Hernandez-Alonso M. D., Maira A. J., Martinez-Arias A., Fernandez-Garcia M., Conesa J. C. and Soria J., Chem. Commun., **24** 2718 (2001).

Gratzel M., Comments Inorg. Chem. **12** 13 (1991).

Hohenberg P. and Kohn W., Phys. Rev. **136** B864 (1964).

Horn M., Schwerdtfeger C. F. and Meagher E. P., Z. Kristallogr. **136** 273 (1972)

Howard C. J., Sabine T. M. and Dickson F., Acta Crystallogr., Sect. B: Struct. Sci. **47** 462 (1991).

http://groups.msn.com/100Mexican/chm494specialprojecttitaniumdioxidesolarcells.msnw sept 2006

http://roger.ecn.purdue.edu/~propulsi/propulsion/comb/propellants.html Sept 2006

http://simplethinking.com/dunn/ch22/anatase.stm Oct 2006

Jurek K., Guglielni M., Kuncova K., Renner O., Lukes F., Navratil M., Rousky E., Vorlicek V. and Kokesova K., J. Mater Sci. **27** 2549 (1992).

Kohn W. and Sham L. J., Phys. Rev. **140** A1133 (1965).

Lagarec K. and Desgreniers S., Solid State Commun. **94** 519 (1995).

Lin Z., Orlov A., Lambert R. M. and Payne M. C., J. Phys. Chem. B **109** 20948 (2005).

Maruska H.P. and Ghosh A.K., Sol. Energy **20** 443 (1978).

Mo S. D. and Ching W. Y., Phys. Rev. B **51** 13 023 (1995).

Murnaghan F.D., 'The Compressibility of Media under Extreme Pressures', in Proceedings of the National Academy of Sciences **30** 244 (1944).

Muscat J., Swamy V. and Harrison N. M, Phys. Rev. B **65** 224112 (2002).

Nakayama T., Onisawa K., Fuyama M. and Hanasono M., J. Electrochem. Soc. **139** 1204 (1992).

Ollis D. F., and Al-Ekali H. (eds), Photocatalyic purification and treatment of water and air, Elsevier, Amsterdam, (1993).

Park M. S., Kwon S. K. and Min B. I., Phys. B **328** 120 (2003).

Park M. S., Kwon S. K. and Min B. I., Phys. Rev. B **65** 161201 (2002).

Payne M. C., Teter M. P., Allan D. C., Arias T. A. and Joannopoulos J. D., Rev. Mod. Phys. **64** 1045 (1992).

Perdew J. P. and Wang Y., Phys. Rev. B **45** 13 244 (1992).

Peters T. A., Peters J. J., Koestler R. and Grube C. H., Minerals of the Buckwheat dolomite, Franklin, New Jersey. Mineralogical Record, 14, 183 (1983).

Swamy V. and Dubrovinsky L. S., J. Phys. and Chem. of solids, **62** 673 (2001a).

Swamy V. Gale J. D. and Dubrovinsky L. S., J. Phys. and Chem. of solids, **62** 887 (2001b).

Tang H., Berger H., Schmid P. E. and Levy F., Sol. States Commun. **92** 267 (1994b).

Tang H., Prasad K., Sanjines R., Schmid P. E. and Levy F., J. Appl. Phys. **75** 2042 (1994a).

Tang H., Schmid P. E., Berger H., Burri G. and Levy F., Solid State Commun. **87** 847 (1993).

Thomas L. H., Proc. Camp. Philos. Soc. **23** 542 (1926).

Wimmer E., Freeman A. J.,Fu C. L., Cao P. L., Chou S. H. and Delly B., in Jensen and Truhlar (eds). D. G., Supercomputer Research in chemistry and chemical Engineering. Acs Symposium Series **353** 49 (1987).

# Appendix A

# Publications

M. G. Matshaba and P. E Ngoepe, Electronic and optical properties of pure and M doped anatase $TiO_2$ (M= Pt, Au, Ag and Pd), Material Modelling Centre, Department of Physics, University of Limpopo (Turfloop Campus), SA. To be published soon.

# Appendix B

## Papers presented at the conferences

M.G. Matshaba et al.," Modelling studies of optical properties and the partial density of states for $TiO_2$ (anatase structure)". Presented at interscience 2003, in October 2003 at the University of the North.

M.G. Matshaba et al." Structural and optical properties of pure $TiO_2$ (anatase) and transitional elements doped anatase". Presented at South African Institute of Physics (SAIP) $49^{th}$ Annual Conference, in July 2004 at the University of the Free State.

M.G. Matshaba et al.," Computational studies of structural and optical properties of pure $TiO_2$ (anatase structure)". Presented at Materials Modelling Centre $8^{th}$ Annual Conference, in March 2004 at the University of the North.

M.G. Matshaba et al., "Computational study of properties of $TiO_2$ anatase structure and doped anatase". Presented at South African Institute of Physics (SAIP) $50^{th}$ Annual Conference, in July 2005 at the University of Pretoria.